

# Ultrafast Dynamics of Electronic Resonances in Molecules Adsorbed on Metal Surfaces: A Wave Packet Propagation Approach

Fernando Aguilar-Galindo, Andrey G. Borisov, and Sergio Díaz-Tendero\*



Cite This: *J. Chem. Theory Comput.* 2021, 17, 639–654



Read Online

ACCESS |

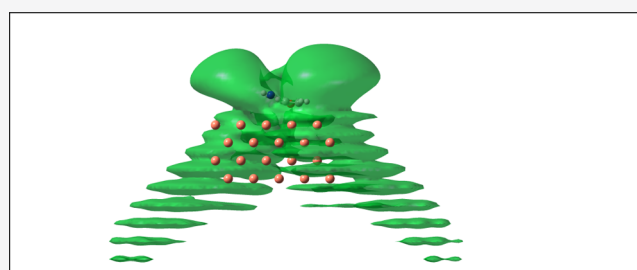


Metrics & More



Article Recommendations

**ABSTRACT:** We present a wave packet propagation-based method to study the electron dynamics in molecular species in the gas phase and adsorbed on metal surfaces. It is a very general method that can be employed to any system where the electron dynamics is dominated by an active electron and the coupling between the discrete and continuum electronic states is of importance. As an example, one can consider resonant molecule–surface electron transfer or molecular photoionization. Our approach is based on a computational strategy allowing incorporating ab initio inputs from quantum chemistry methods, such as density functional theory, Hartree–Fock, and coupled cluster. Thus, the electronic structure of the molecule is fully taken into account. The electron wave function is represented on a three-dimensional grid in spatial coordinates, and its temporal evolution is obtained from the solution of the time-dependent Schrödinger equation. We illustrate our method with an example of the electron dynamics of anionic states localized on organic molecules adsorbed on metal surfaces. In particular, we study resonant charge transfer from the  $\pi^*$  orbitals of three vinyl derivatives (acrylamide, acrylonitrile, and acrolein) adsorbed on a Cu(100) surface. Electron transfer between these lowest unoccupied molecular orbitals and the metal surface is extremely fast, leading to a decay of the population of the molecular anion on the femtosecond timescale. We detail how to analyze the time-dependent electronic wave function in order to obtain the relevant information on the system: the energies and lifetimes of the molecule-localized quasistationary states, their resonant wavefunctions, and the population decay channels. In particular, we demonstrate the effect of the electronic structure of the substrate on the energy and momentum distribution of the hot electrons injected into the metal by the decaying molecular resonance.



Ultrafast resonant charge transfer from the  $\pi^*$  orbital of acrylamide decaying towards a metal surface

## 1. INTRODUCTION

Standard methods in quantum chemistry are typically employed to study static properties or bound states of systems where the Hamiltonian is a time-independent operator. For the phenomena involving discrete states coupled with a continuum, even though the stationary scattering matrix, filter diagonalization, or complex scaling approaches were developed,<sup>1–5</sup> the evolution of the computing capacities triggered a fast development of wave packet propagation (WPP) techniques.<sup>6–13</sup> The WPP explicitly solves the time-dependent Schrödinger equation (TDSE), and, combined with wave function representation on the spatial grid, allows efficiently accounting for the continuum effects. Moreover, the WPP naturally allows considering quantum systems under the action of the explicitly time-dependent Hamiltonians as relevant for the attosecond science,<sup>14–16</sup> for example. In the past few decades, many problems in Physics and Chemistry have been thus addressed with WPP techniques (see e.g., refs 17–26).

In this work, we present a WPP-based methodology to study those systems where molecule-localized electronic states are coupled with a continuum of propagating electronic states, as

in the case of the photoionization, or for a single molecule adsorbed on a metal surface, as specifically addressed here. Our purpose is to merge (i) an ab initio description of the molecular electronic structure as provided by quantum chemistry approaches; and (ii) the possibility to describe the continuum states without artificial quantization, that is, imposing the outgoing wave boundary conditions as offered by WPP. As a case study, we address the negative ion states of organic molecules adsorbed on metal surfaces. In such systems, an electron initially localized on a molecular orbital can escape into the continuum of metal electronic states via energy-conserving resonant electron transfer; the so-called resonant charge transfer (RCT) process. The molecule-localized

Received: September 30, 2020

Published: January 28, 2021



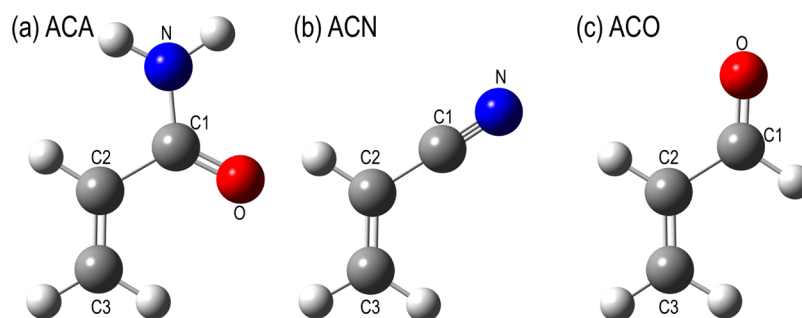


**Figure 1.** Three vinyl derivative molecules studied in the present work: (a) ACA, (b) ACN, and (c) ACO. Figure was also published in refs.<sup>63,64</sup>

electronic states broaden into resonances, with lifetimes given by the rate of the RCT. This is a typical example of discrete state-continuum coupling, which admits a theoretical description within the single electron picture.

Because of the possible applications of the adsorbed molecules as single photon sources,<sup>27–30</sup> and because of the role played by adsorbate-localized electronic states in surface reactivity (see e.g.,<sup>31–37</sup>), the characterization of the adsorbate-induced anion or excited state resonances at metal surfaces is of paramount importance. In particular, the lifetime of a molecular state is a key property, which controls the efficiency of the reaction mechanism where the too short lifetime would not allow for an energy transfer between electrons and nuclei.<sup>38–40</sup> Similar, too fast electron transfer from an excited state into the substrates would hinder the decay via photon emission.<sup>41,42</sup> With the methodology presented in this work, one can obtain a complete characterization of the resonances: energy, lifetime, and resonant wavefunction.

From the experimental point of view, the electron dynamics in excited states at surfaces has been thoroughly addressed using the proximal probe scanning tunneling microscopy (STM) technique<sup>43–46</sup> as well as the time-resolved two-photon-photoemission.<sup>13,47–50</sup> These and other experiments triggered large theoretical interest. Among other theoretical approaches, the excited-state potential-energy surfaces for molecules adsorbed on metal substrates were obtained using the  $\Delta$  self-consistent field ( $\Delta$ SCF) method<sup>51</sup> and the  $\Delta$ SCF density-functional theory ( $\Delta$ DFT).<sup>52,53</sup> The WPP technique has also been applied to study energies and lifetimes of the excited electronic states localized on adatoms, adlayers, and on small nanostructures.<sup>54–61</sup> Rather simple model descriptions of the system have been used in these early works based on the WPP technique. Recently, RCT between single molecular adsorbates and semiconductor surfaces has been addressed at the ab initio level;<sup>62</sup> however, within the stationary Green's function framework that does not admit time-dependent Hamiltonians.

The WPP method reported here aims simultaneously: (i) to represent the continuum of the propagating electronic states inside the metal and in the vacuum region, and (ii) to fully account for the electronic structure of the adsorbed molecule using potentials obtained with quantum chemistry calculations. We illustrate our approach with a complete description of the quasistationary molecular anion-localized states (resonances) for the three vinyl derivatives: acrylamide (ACA), acrylonitrile (ACN), and acrolein (ACO) adsorbed on a Cu(100) surface. The structure of these molecules is shown in Figure 1. We obtain the resonance decay channels and wave function, as well as the resonance energy and the decay rate associated with its lifetime. The above-mentioned molecules are characterized by

an antibonding  $\pi^*$   $C_2$ – $C_3$  character of the lowest unoccupied molecular orbital (LUMO) orbital. Thus, the negative ion formation by, for example, an electron injection from an STM tip or via attachment of a hot electron from the metal would weaken the (formally) double  $C=C$  bond, activating this bond. On the other hand, one would expect that the  $\pi^*$  orbitals strongly hybridize with the metal surface,<sup>63</sup> leading to a fast decay of the negative ion population. Thus, understanding the dynamics of such electronic resonances provides also information on the catalytic activity of such states.

It is worth stressing that our developed software is able to go well beyond the problem of the RCT at metal surfaces and to deal with general problems of electron escape from molecular system into a continuum, including the case of the time-dependent Hamiltonians as in photoionization. In particular, using the all valence-electron description provided by standard quantum chemistry packages (as the ones used here, see below) makes it possible to address the electron-rescattering processes. This subject is of great interest for the formation of photoemission delays in attosecond science or for the molecular imaging in optical field emission with intense laser pulses.<sup>15,16,65–68</sup>

This article is organized as follows. Next section presents the methodology: solution of the TDSE using the WPP scheme, the strategy to construct the potential of the active electron, and the extraction of the relevant information from the propagation. Section 3 is devoted to the results: characterization of anion resonances localized on vinyl derivatives adsorbed on a Cu(100) surface. We end the article with the conclusions in Section 4. Atomic units are used throughout the article unless otherwise stated.

## 2. METHODOLOGY

**2.1. Time-Dependent Schrödinger Equation.** The WPP approach consists in solution of the time TDSE describing the time evolution of the wave function,  $\Psi(\vec{r}, t)$ , of the active electron.  $\Psi(\vec{r}, t)$  is sought as function of time and spatial coordinates  $\vec{r}$ , and evolves in time according to

$$i\frac{\partial}{\partial t}\Psi(\vec{r}, t) = \hat{H}(t)\Psi(\vec{r}, t) \quad (1)$$

where  $\hat{H}(t)$  is the Hamiltonian of the system. At this stage for the sake of completeness, we consider the case of the time-dependent Hamiltonian. Given an initial condition  $\Psi_0(\vec{r}) \equiv \Psi(\vec{r}, t = 0)$ , the solution of eq 1 is given by

$$\Psi(\vec{r}, t) = \hat{U}(t)\Psi_0(\vec{r}) = \hat{\mathcal{P}} e^{-i\int_0^t \hat{H}(t')dt'}\Psi_0(\vec{r}) \quad (2)$$

where  $\hat{U}$  is the time evolution operator, and  $\hat{\mathcal{P}}$  is the time ordering operator.

Numerically, many time-propagation schemes have been developed including the global and short-time propagation techniques.<sup>6–9,69–75</sup> Here, we prefer the short-time propagation approach for its versatility in addressing the time-dependent and time-independent Hamiltonians as well as for the availability of the information on the system in due course of the time evolution. Setting propagation time-step  $\Delta t$ , the time evolution is obtained from

$$\Psi(\vec{r}, t + \Delta t) = e^{-i\Delta t \hat{H}(t + \frac{\Delta t}{2})} \Psi(\vec{r}, t) \quad (3)$$

The Hamiltonian  $\hat{H}$  of the system can be expressed in the following general form

$$\begin{aligned} \hat{H}(t) &= \hat{T} + \frac{V(\vec{r}, t) + \hat{V}_{\text{NL}} + V_{\text{abs}}(\vec{r})}{\hat{V}_{\text{tot}}(t)}, \\ \hat{T} &= -\frac{1}{2} \vec{\nabla}^2, \\ \hat{V}_{\text{NL}} &= \sum_{\alpha} v_{\alpha} \hat{P}_{\alpha} = \sum_{\alpha} |\phi_{\alpha}\rangle v_{\alpha} \langle \phi_{\alpha}| \end{aligned} \quad (4)$$

Here,  $\hat{T}$  is the kinetic energy operator and  $\hat{V}_{\text{tot}}(t)$  is the total (possibly time-dependent) potential. It consists of the several contributions described below in the order of appearance.

The local potential  $V(\vec{r}, t)$ , includes the local part of the electron–molecule interaction, the electron–surface interaction, which takes into account the charge transfer between the molecule and the substrate, and, finally, the possible external potentials acting on the system. As an example, an incident electromagnetic pulse with electric field  $\vec{E}(t)$  contributes to the local potential with the term  $\vec{E}(t) \cdot \vec{r}$ . Although in this work, we do not consider any external time-dependent potential acting on the system, the code is ready to use this option. The details of the electron–molecule and the electron–surface interactions are given in the following sections.

The nonlocal (local) potential,  $\hat{V}_{\text{NL}}$ , arises from the pseudopotential description of the molecular electronic structure as often implemented in the DFT simulations.<sup>76–78</sup> It is defined by the projectors  $\hat{P}_{\alpha}$  on the orthonormal basis of  $\phi_{\alpha}$ -states, and by the set of constants  $v_{\alpha}$ . In the  $\vec{r}$  representation, the action of the projector on the wave function  $\Psi(\vec{r}, t)$  is defined as:  $\hat{P}_{\alpha} \Psi(\vec{r}, t) = v_{\alpha} \phi_{\alpha}(\vec{r}) \int \phi_{\alpha}(\vec{r}') \Psi(\vec{r}', t) d^3r'$ . In the present case  $\phi_{\alpha}(\vec{r})$  is a real function.

Finally,  $V_{\text{abs}}(\vec{r})$  is the local complex absorbing potential (CAP) used to impose the outgoing wave conditions at the boundaries of the computational box consistent with bound state-continuum interaction at the focus of the present study.

Because different operators contributing to the Hamiltonian of the system do not commute in general, the short-time propagation given by eq 3 is performed using the split operator technique<sup>6,7,69,73</sup>

$$\begin{aligned} \Psi(\vec{r}, t + \Delta t) &= \underbrace{e^{-i\frac{\Delta t}{2} V_{\text{abs}}} e^{-i\frac{\Delta t}{2} V(t')} e^{-i\frac{\Delta t}{2} \hat{V}_{\text{NL}}}}_{\hat{U}_{\text{L}}} e^{-i\Delta t \hat{T}} \\ &\times \underbrace{e^{-i\frac{\Delta t}{2} \hat{V}_{\text{NL}}} e^{-i\frac{\Delta t}{2} V(t')} e^{-i\frac{\Delta t}{2} V_{\text{abs}}}}_{\hat{U}_{\text{R}}} \Psi(\vec{r}, t) \end{aligned} \quad (5)$$

where  $t' = t + \frac{\Delta t}{2}$  the propagation error is of the order of  $\Delta t^3$ .

The reason why it is convenient to split the Hamiltonian in terms of kinetic energy and local and nonlocal potential terms

lies in the fact that a local operator (as the potential energy operator) is diagonal in a direct space while the kinetic energy operator is diagonal in the reciprocal space. We then use the Fourier grid Hamiltonian (FGH) approach to perform the time propagation of the wave function.<sup>6,8,9,69,70,79</sup> The wave function of the active electron is represented on a discrete equidistant grid in Cartesian coordinates. The action of the exponential of the local potentials is computed in the direct space by direct multiplication on each grid point. The action of the exponential of the kinetic energy operator is computed in the reciprocal space leading to the following algorithm of the time step

$$\Psi(\vec{r}, t + \Delta t) = \hat{U}_{\text{L}} \mathcal{F}^{-1} [e^{-i\Delta t T_{\vec{k}}} \mathcal{F} [\hat{U}_{\text{R}} \Psi(\vec{r}, t)]] \quad (6)$$

Here,  $\mathcal{F}$  ( $\mathcal{F}^{-1}$ ) stands for the direct (inverse) fast Fourier transform (FFT). With absolute value of the momentum  $k^2 = k_x^2 + k_y^2 + k_z^2$ , the diagonal kinetic energy matrix  $T_{\vec{k}}$  is given by

$$T_{\vec{k}} = \frac{1}{2} k^2, \quad k_{x,y,z} = \frac{2\pi j_{x,y,z}}{N_{x,y,z} h_{x,y,z}} \quad (7)$$

where  $N_{x,y,z}$  and  $h_{x,y,z}$  are the number of knots and the step of the mesh in the corresponding direction. The index  $j_{x,y,z}$  runs in the limits  $-(N_{x,y,z}/2 - 1) \leq j_{x,y,z} \leq N_{x,y,z}/2$ .

If the Hamiltonian does not contain any time-dependent term, this scheme is very efficient because the exponentials have to be calculated once at the beginning of the calculation and the FFT algorithm is employed to switch between representations.

Before closing this section, we discuss the computation of the exponential  $e^{-i\hat{V}_{\text{NL}}\Delta t/2}$  of the nonlocal operator  $\hat{V}_{\text{NL}}(\vec{r})$  defined using eq 4. Because the  $|\phi_{\alpha}\rangle$  states are orthonormal  $\langle \phi_{\alpha'} | \phi_{\alpha} \rangle = \delta_{\alpha'\alpha}$  the operators  $\hat{P}_{\alpha}$  commute. Then,

$$e^{-i\frac{\Delta t}{2} V_{\text{NL}}} = e^{-i\frac{\Delta t}{2} \sum_{\alpha} v_{\alpha} \hat{P}_{\alpha}} = \prod_{\alpha} e^{-i\frac{\Delta t}{2} v_{\alpha} \hat{P}_{\alpha}} \quad (8)$$

Using the Taylor expansion of the exponent  $e^{-i\frac{\Delta t}{2} v_{\alpha} \hat{P}_{\alpha}} = 1 + \sum_{n=1}^{\infty} \frac{(-i\frac{\Delta t}{2} v_{\alpha})^n}{n!} \hat{P}_{\alpha}$ , we finally obtain

$$e^{-i\frac{\Delta t}{2} V_{\text{NL}}} = 1 + (e^{-i\frac{\Delta t}{2} v_{\alpha}} - 1) \hat{P}_{\alpha} \quad (9)$$

**2.2. Potential. 2.2.1. Molecular Potential.** One of the most important advantages of the present methodology is that it incorporates the versatile character of the WPP on real space grids in describing the propagating continuum states, and the full account for the realistic electronic structure of the adsorbed molecule. The description of the interaction between an active electron and the molecule is thus at the core of our approach, where the required information is extracted from quantum chemistry packages. In this case, the molecular potential contains local and nonlocal components described below.

The main idea is that in the WPP code, we use exactly the same potential as the one leading to the ground-state Kohn–Sham (KS) orbitals within the DFT software applied to the same molecule. This guarantees that, for the free-standing molecule, the KS orbitals calculated using DFT are also the eigenstates of the FGH driving the electron dynamics in WPP. For the electron–nuclei interaction, the standard DFT packages routinely employ the frozen core approximation and pseudopotentials in order to decrease the computational effort. For the WPP, only norm conserving pseudopotentials

can be applied in order to guarantee the unitarity of the time propagation operator and thus preservation of the norm of the wave packet. Thus, the Abinit package<sup>77,78,80–82</sup> is an excellent choice for our approach, because it employs norm-conserving pseudopotentials.<sup>83</sup> These pseudopotentials contain the local part  $V_j^{\text{loc}}$  and the nonlocal part  $V_j^{\text{nl}}$  that is responsible for the correct energy position of the calculated electronic states. Index  $j$  stands for the given atom within the molecule, which implies that prior to the WPP study the molecular structure, defined by the set of atomic positions  $\{\vec{r}_j\}$ , has to be determined from the ground-state ab initio calculations for the molecule in a given environment. Depending on the problem at hand, these calculations can be performed for the free standing molecule using the Gaussian09<sup>84</sup> package or, for the molecule adsorbed at metal surface, the VASP<sup>85–87</sup> package.

Provided atomic positions, the nonlocal potential is given using

$$\hat{V}_j^{\text{nl}} = \sum_f |\phi_{f,j}\rangle v_{f,j} \langle \phi_{f,j}| \quad (10)$$

where  $\langle \phi_{f,j} | \phi_{f',j} \rangle = \delta_{ff'}$ . An index  $f$  runs over the angular momentum and magnetic quantum number of each pseudofunction. It also takes into account the situations where several pseudofunctions are needed for the atom  $j$ .  $v_{f,j}$  is the shift in the energy of the (normalized) eigenfunction  $\phi_{f,j}$  that places the corresponding eigenstate at the correct position in the spectrum. Note that because  $\phi_{f,j}$  are localized in the region of the space surrounding the corresponding atom, projection of the time-dependent wave function required to perform the propagation time step (see eq 9) only involves the integrations within the small portion of the complete three-dimensional (3D) mesh.

The interaction between an active electron and the rest of the molecular electrons is obtained from the Abinit calculations using the previously optimized molecular structure defined by  $\{\vec{r}_j\}$ . The resulting local potential is given by the sum of the Hartree,  $V_H^{\text{Mol}}(\vec{r})$  and exchange–correlation,  $V_{\text{xc}}^{\text{Mol}}(\vec{r})$ , potentials that are calculated on the knots of the WPP grid.

Despite the huge improvements in the development of functionals, the DFT approaches are far from a correct description of the excited states, electron affinities, or ionization energies in terms of the Koopmans' theorem.<sup>88</sup> This is while the lifetime of the quasi-stationary states localized on adsorbed molecule considered here is determined by their energy position with respect to the features of the band structure of the substrate. Similarly, if one is interested in the photodetachment from the molecular anion, the energy of the affinity level with respect to the vacuum is of paramount importance.

To impose the correct electron affinity in the WPP calculations, we proceed as follows. First, for the molecular structure defined by  $\{\vec{r}_j\}$ , the electron affinity  $E_a$  is calculated with a very high accuracy as the energy difference of the free-standing anion and the free-standing neutral molecule, using CCSD (coupled cluster theory including single and double excitations) and a triple- $\zeta$  basis in both cases. To this end, the Gaussian09<sup>84</sup> is used. Furthermore, we consider that for the molecular anion, the wave function of an external electron is close to the wave function of the LUMO orbital of the neutral molecule,  $\Phi_{\text{LUMO}}(\vec{r})$ . Then, the nonlocal potential

$$\hat{V} = U |\Phi_{\text{LUMO}}\rangle \langle \Phi_{\text{LUMO}}| \quad (11)$$

is added to the electron–molecule interaction. The constant  $U = -E_a - E_{\text{LUMO}}$  provides the energy correction given by the difference between the KS energy of the LUMO,  $E_{\text{LUMO}}$ , and the electron affinity  $E_a$  of the molecular anion obtained from the high level ab initio calculations. The energy,  $E_{\text{LUMO}}$ , and wave function of the LUMO orbital,  $\Phi_{\text{LUMO}}(\vec{r})$ , are calculated using the WPP (see below) for the electron–molecule interaction given using the potential

$$\hat{V}_{\text{Abinit}} = V_H^{\text{Mol}}(\vec{r}) + V_{\text{xc}}^{\text{Mol}}(\vec{r}) + \sum_j V_j^{\text{loc}} + \sum_j \hat{V}_j^{\text{nl}} \quad (12)$$

extracted from the Abinit calculations. It is worth noting that for converged WPP calculations, the KS energy of the LUMO obtained in Abinit and the WPP results differ by less than 0.1 meV.

Summarizing the discussion above, the final potential of the interaction between an active electron and the molecule reads

$$\hat{V}_{\text{Mol}} = V_H^{\text{Mol}}(\vec{r}) + V_{\text{xc}}^{\text{Mol}}(\vec{r}) + \sum_j V_j^{\text{loc}} + \sum_j \hat{V}_j^{\text{nl}} + \hat{V} \quad (13)$$

where the summation in  $j$  runs over all atoms forming the molecule. This choice guarantees that for the free-standing molecule with atomic arrangement  $\{\vec{r}_j\}$ , the Hamiltonian

$$H = -\frac{1}{2} \vec{\nabla}^2 + \hat{V}_{\text{Mol}} \quad (14)$$

projected on the grid leads within the WPP scheme to the existence of the stationary state  $\Phi_{\text{LUMO}}(\vec{r})$  at the energy  $-E_a$ . We note here that the total nonlocal potential in eq 5 is given by

$$\hat{V}_{\text{NL}} \rightarrow \hat{V}_{\text{NL}}^{\text{Tot}} = \sum_j \hat{V}_j^{\text{nl}} + \hat{V} \quad (15)$$

The nonlocal operators  $\hat{V}_j^{\text{nl}}$  and  $\hat{V}$  do not commute. As a consequence, if the energy correction to the orbitals of the ground state neutral molecule is applied, the calculation of the exponential of the nonlocal potential in eq 5 requires an additional split

$$e^{-i\frac{\Delta t}{2} \hat{V}_{\text{NL}}^{\text{Tot}}} = e^{-i\frac{\Delta t}{4} \hat{V}} \left[ \prod_j e^{-i\frac{\Delta t}{2} \hat{V}_j^{\text{nl}}} \right] e^{-i\frac{\Delta t}{4} \hat{V}} + O(\Delta t)^3 \quad (16)$$

It is also worth noting that the Abinit calculations explicitly account not only for the external, but for the tightly bound molecular orbitals. The resulting strong and localized on atomic positions potential represents a complication because the tight WPP mesh and relatively small propagation time step are required to describe the corresponding wave functions quickly changing close to atomic positions. On the other hand, this description of the electron–molecule interaction allows one to use the present methodology to address, for example, the scattering of the energetic electrons penetrating close to the atomic cores. This subject is of great interest for the strong field and/or ultrafast science.

**2.2.2. Interaction with the Metal Surface.** For the molecules adsorbed at metal surfaces, the total potential that drives the dynamics of the active electron is determined by the electron–molecule and electron–substrate interactions. In



order to account for a proper adsorption geometry, we obtain the interaction potential between the active electron and the metal as follows.

- Using VASP, by combining DFT and projected augmented wave (PAW) pseudopotentials, we perform the calculation of the adsorption geometry. During these geometry optimizations, all the metal coordinates, but the  $z$  coordinate of the atoms in the first layer, are fixed; and the atomic positions of the molecule are allowed to be relaxed.
- Then, the determined adsorption geometry of the molecule given by atomic positions  $\{\vec{r}_j^{\text{Ads}}\}$  is used in the single Abinit run describing the molecule adsorbed on a metal surface and allowing to obtain the electronic density as well as the potential of the entire system  $\hat{V}_{\text{Met+Mol}}^{\text{DFT}}$ .
- Abinit calculations are also performed for the bare metal surface where the first layer is fixed at the positions determined for the adsorption case. This calculation provides with  $\hat{V}_{\text{Met}}^{\text{DFT}}$ , the electron–metal interaction potential.
- Abinit calculations are finally performed for the free-standing molecule with atomic arrangement given by  $\{\vec{r}_j^{\text{Ads}}\}$ , which provides the electron–molecule interaction potential  $\hat{V}_{\text{Mol}}$ .

The potential of the system can be then expressed as

$$\hat{V}_{\text{Met+Mol}}^{\text{DFT}} = \hat{V}_{\text{Mol}} + \hat{V}_{\text{Met}}^{\text{DFT}} + \Delta V_{\text{Met+Mol}}^{\text{DFT}}(\vec{r}),$$

$$\Delta V_{\text{Met+Mol}}^{\text{DFT}}(\vec{r}) = V_{\text{Met+Mol}}^{\text{DFT}}(\vec{r}) - \hat{V}_{\text{Mol}} - \hat{V}_{\text{Met}}^{\text{DFT}} \quad (17)$$

Note that by construction,  $\Delta V_{\text{Met+Mol}}^{\text{DFT}}$  is a local potential mainly determined by the valence electrons. The contribution of the inner shell electrons is nearly cancelled, while the pseudopotentials are cancelled exactly. The potential  $\Delta V_{\text{Met+Mol}}^{\text{DFT}}$  then originates from the difference between the electron density of the entire system and the sum of the electron densities of the individual components leading to the corresponding difference in the Hartree and exchange correlation potentials. This approach has to be considered with care. Strictly speaking, it is well justified only if the surface reconstruction associated with the molecular adsorption is small. Because the effect of an adsorbed molecule is quickly screened inside the metal and at some nm of the lateral separation, the potential  $\Delta V_{\text{Met+Mol}}^{\text{DFT}}$  is nonzero only in the vicinity of the molecule, as follows from the results shown in Figure 2. Thus, an active electron moving in the asymptotic region at large lateral separations or deep inside the metal experiences only the potential of the metal  $\hat{V}_{\text{Met}}^{\text{DFT}}$ .

Because  $\Delta V_{\text{Met+Mol}}^{\text{DFT}}$  vanishes in the asymptotic region, we can introduce an approximation that greatly reduces the computational load and makes the problem of the quasistationary states localized on the single adsorbed molecule, and decaying into the metal, numerically accessible. Indeed, the standard codes based on DFT are able to deal with enough atoms to describe properly many of the processes of interest such as molecular adsorption geometry, formation of molecule–metal bond, and so forth.<sup>89–102</sup> Typically, 4–5 atomic layers are enough for a proper description of these properties, provided a large enough supercell in the lateral direction so that the effects owing to periodic representation of the system inherent to this codes can be neglected. However, if one is interested in the decay of molecule localized states into the metal, or in the photo-

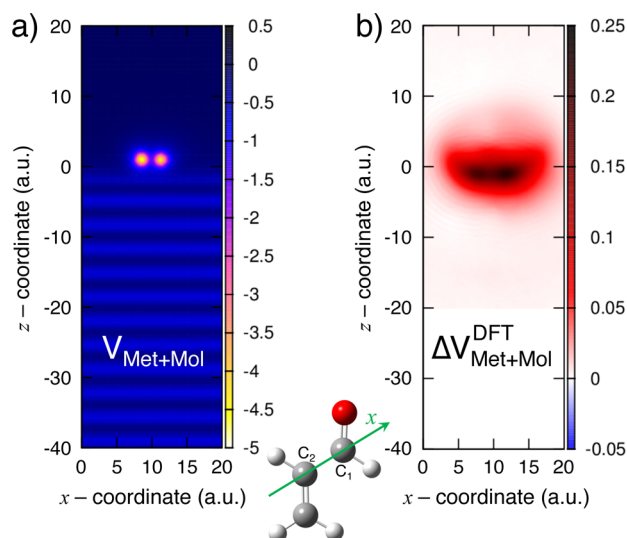


**Figure 2.** (a) Local part of the model potential  $\hat{V}_{\text{Met+Mol}}$  (see eq 18) for the electron active in the RCT between the ACO anion and the Cu(100) surface. (b) Difference  $\Delta V_{\text{Met+Mol}}^{\text{DFT}}$  between the electron interaction potential with ACO molecule adsorbed on the Cu(100) surface and the sum of the independent electron/ACO and electron/Cu(100) interaction potentials. Here, all potentials are calculated using the DFT as implemented in the Abinit package. The potential maps in panels (a,b) are presented in the  $(x, z)$ -plane. The  $x$ -coordinate runs along the  $C_1$ – $C_2$  bond as indicated in the inset. The  $z$ -coordinate is perpendicular to the surface,  $z = 0$  corresponds to the surface Cu atom layer, and the metal is located at negative  $z$  values. The numbers on the vertical color bar in each panel give the potential in atomic units and define the color scale.

emission, the computational domain has to be extended parallel to the surface as well as deep inside the metal and into the vacuum. This is mandatory in order to correctly capture the band structure effects on the electron propagation (e.g., to have fully developed projected band gaps) as well as to avoid the quantization of the continuum of the propagating states in metal and in vacuum. Such an extension of the computational domain requires extremely heavy ab initio calculations in order to generate  $\hat{V}_{\text{Met+Mol}}^{\text{DFT}}$  potential as well as it harms the efficiency of the WPP approach that has to deal with nonlocal potentials at each lattice site of the metal. Of course, if the system of interest is periodic (e.g., self-assembled monolayers), the periodicity of the DFT cell is correct and thus the total cell in the WPP must have the same size; this, however, does not remove the necessity of the large computational domain in the direction perpendicular to the surface.

The way to cope with the problem outlined above consists in replacing the potential obtained from quantum chemistry calculations,  $\hat{V}_{\text{Met+Mol}}^{\text{DFT}}$  by the model potential,  $\hat{V}_{\text{Met+Mol}}$  that preserves an accurate description of the adsorption region while allowing an easy extension of the computational domain. Equation 17 then takes the form

$$\hat{V}_{\text{Met+Mol}} = \hat{V}_{\text{Mol}} + V_{\text{Met}}^{\text{model}}(\vec{r}) + \Delta V_{\text{Met+Mol}}^{\text{DFT}}(\vec{r}) \quad (18)$$

In this case, all local environments of the adsorbed molecule are represented with potentials extracted from the ab initio calculations  $\hat{V}_{\text{Mol}} + \Delta V_{\text{Met+Mol}}^{\text{DFT}}$ , and the metal is represented with an analytical model potential  $V_{\text{Met}}^{\text{model}}(\vec{r})$ , which allows an easy spatial extension of the WPP mesh. We use the model potential developed by Chulkov et al.,<sup>103</sup> successfully applied in the past to describe the dynamics of the excited states at

metal surfaces.<sup>13,48–50,104</sup> This model potential only depends on the electron coordinate  $z$  perpendicular to the surface:  $V_{\text{Met}}^{\text{model}}(\vec{r}) = V_{\text{Met}}^{\text{model}}(z)$ . It smoothly joins the image potential tail of the electron/surface interaction in vacuum and shows the periodic oscillations corresponding to the interaction of the electron with the metal layers inside the bulk, as shown in Figure 3. The periodicity of the potential reflects the

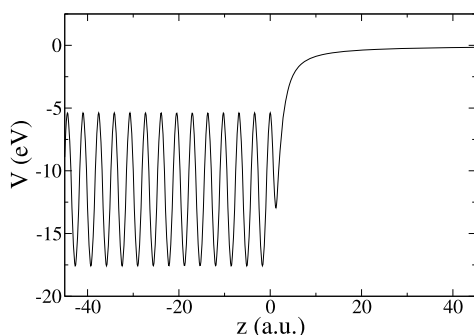


**Figure 3.** Model potential for the Cu(100) surface,<sup>103</sup>  $V_{\text{Met}}^{\text{model}}(\vec{r})$ . The electron/Cu(100) interaction potential is shown as a function of the electron coordinate perpendicular to the surface,  $z$ , where  $z = 0$  corresponds to the surface layer of Cu atoms. The  $z$ -axis points from metal to vacuum with negative  $z$  inside the metal.

arrangement of atomic planes perpendicular to the surface and a free-electron motion parallel to the surface is assumed. Despite its simplicity,  $V_{\text{Met}}^{\text{model}}(z)$  allows correctly recovering the surface electronic structure at the  $\bar{\Gamma}$  point with correct energies for the surface and image potential states, as well as for the projected band gap.<sup>103</sup> The latter is very important for the decay of the electronic resonances at surfaces as it determines the final states in the conduction band available for the RCT process as we discuss below in this article.

In Figure 2, we show the 2D maps of the local part of the potential  $\hat{V}_{\text{Met+Mol}}$  as well as the difference potential  $\Delta V_{\text{Met+Mol}}^{\text{DFT}}(\vec{r})$  for the case of the ACO molecule adsorbed on the Cu(100) surface. As explained above in this subsection,  $\Delta V_{\text{Met+Mol}}^{\text{DFT}}(\vec{r})$  expresses the difference between the DFT results obtained using the Abinit package for the coupled molecule + surface system and sum of the independent electron interactions with and individual molecules and the pristine Cu(100) surface. Two bright regions in Figure 2a arise because of the electron interaction with carbon atoms forming the  $\text{C}_1\text{--}\text{C}_2$  bond, and the periodic oscillations of the potential inside the metal reflect the successive atomic planes parallel to the surface as implemented in the electron–metal interaction potential of ref 103. Notice that the  $\Delta V_{\text{Met+Mol}}^{\text{DFT}}$  potential reaches up to 6 eV, which shows an essential rearrangement of the electron density between the surface and the adsorbed molecule. Obviously, this effect can only be captured by performing the quantum chemistry DFT study for the complete system.

**2.2.3. Complex Absorbing Potentials.** Addressing the decay of the quasistationary state into the continuum of propagating electronic states with the calculations performed on the finite size mesh has been thoroughly addressed in the context of, for example, quantum reaction theory and the theory of resonances.<sup>1–5,8,9,105</sup> Among many techniques proposed in the literature, we use the CAPs that have proven their efficiency for the WPP approaches. The CAPs are introduced at the boundaries of the computational mesh in order to

impose the outgoing wave boundary conditions. In practice, upon arrival to the mesh boundary, an electronic wave packet is progressively absorbed with negligible reflections. Thus, the WPP calculations performed on the finite size mesh are representative for the system in the infinite space.

In practice, we use local CAPs of quadratic form<sup>106</sup> given by

$$V_{\text{abs}}(\vec{r}) = V_{\text{abs}}(x) + V_{\text{abs}}(y) + V_{\text{abs}}(z) \quad (19)$$

where

$$V_{\text{abs}}(\xi) = \begin{cases} -i\lambda_-(\xi - \xi_-)^2 & \text{if } \xi \leq \xi_- \\ -i\lambda_+(\xi - \xi_+)^2 & \text{if } \xi_+ \leq \xi \\ 0 & \text{otherwise} \end{cases} \quad (20)$$

In eq 20, we assume  $\xi_- < \xi_+$ , so that  $\xi_- \leq \xi \leq \xi_+$  is the absorption-free region. Using CAPs results in the non-Hermitian Hamiltonian. The associated nonconservation of the norm of the wave function in WPP reflects the absorption of the electron flux arriving at the mesh boundary as if the electrons were leaving the computation box.

**2.2.4. Total Potential.** For the case of the anion resonances of adsorbed molecules chosen as an example of our approach, the resulting total potential for the WPP as enters eq 4 does not depend on time and it is given using

$$\hat{V}_{\text{tot}} = \hat{V}_{\text{Mol}} + V_{\text{Met}}^{\text{model}}(\vec{r}) + \Delta V_{\text{Met+Mol}}^{\text{DFT}}(\vec{r}) + V_{\text{abs}}(\vec{r}) \quad (21)$$

The electron–molecule interaction potential  $\hat{V}_{\text{Mol}}$  is defined with eq 13.

**2.3. Extracting Lifetimes, Energies, and Resonant Wavefunctions.** All the information on the decaying state is contained in the time-dependent wave-function of the active electron  $\Psi(\vec{r}, t)$ . In this section, we show the typical  $\Psi(\vec{r}, t)$  analysis techniques that allow one to obtain the energy, lifetime, and electronic wave function of the anion resonance localized on adsorbed molecules.

Important quantity to be determined with WPP is the autocorrelation function,  $A(t)$ , given by

$$A(t) = \int \Psi_0^*(\vec{r}) \Psi(\vec{r}, t) d^3\vec{r} \quad (22)$$

where  $*$  stands for the complex conjugate.

The time-to-energy Fourier transform of the autocorrelation function yields the energy-dependent electronic density of states projected on the initial wave function (pDOS)<sup>13</sup>

$$\begin{aligned} n(E) &= \text{Re} \left\{ \int_0^T A(t) e^{i(E+i\eta)t} dt \right\} \\ &= \sum_k |\langle \varphi_k | \Psi_0 \rangle|^2 \delta(E_k - E) \end{aligned} \quad (23)$$

where  $\text{Re}\{Z\}$  stands for the real part of the complex number  $Z$ ,  $T$  is the finite, albeit large propagation time,  $\eta \rightarrow +0$ , and  $|\varphi_k\rangle$  stands for the bound and continuum eigenstates of the Hamiltonian  $\hat{H} = \hat{T} + \hat{V}_{\text{tot}}$  of the system.

The decaying (quasistationary) molecular states appear as resonances in  $n(E)$ . The energy positions and widths of the resonances in  $n(E)$  are associated with energies and RCT decay rates of the corresponding molecular states. The approach above is robust, but it is difficult to apply in the case when the long-lived states are present in the system so that very large propagation times  $T$  are then needed to reach

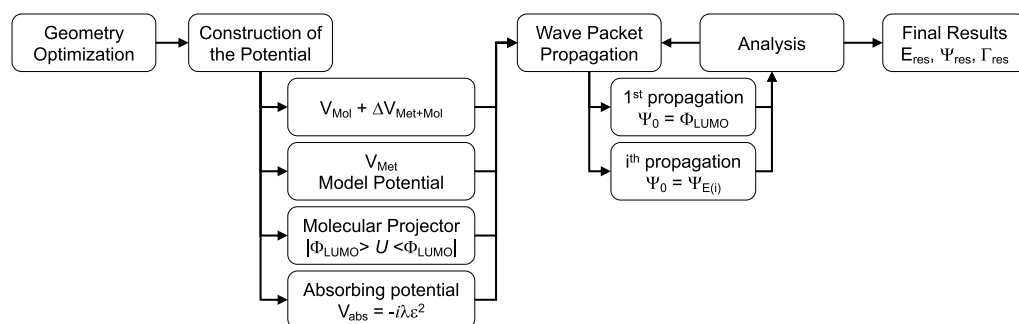


**Figure 4.** Workflow of the computational strategy proposed here. Geometry optimization is followed by the construction of the total potential, including different steps. Once the potential is obtained, WPP simulations are performed. The analysis allows obtaining the final results: energy, lifetime, and resonant wave-function of the state of interest.

convergence in eq 23. In such situations, an alternative scheme is used. The autocorrelation is sought in the form (see ref 13)

$$\mathcal{A}(t) = \sum_{j=1,\dots,n} a_j e^{-iE_j t} e^{-\frac{\Gamma_j}{2}t} \quad (24)$$

that is, it is represented as a linear combination of the contributions from quasistationary states with energies  $E_j$  and decay rates  $\Gamma_j$ . Some of the states are the actual resonances of the system and some are the “effective” resonances that represent the contribution of the conduction band states, surface state continuum, and free-propagating states above the vacuum level. The least square fit of the autocorrelation function  $A(t)$  obtained from the WPP to the analytical form  $\mathcal{A}(t)$  given using eq 24 yields the complex energies ( $E_j$ ,  $\Gamma_j$ ) of the resonances in the system. The results for the actual resonances converge as a function of the propagation time  $T$  and the number of states  $n$ .

Once the energy,  $E_j$ , of the resonance is known, the corresponding wave function of the decaying state can be extracted from

$$\psi^{\text{res}}(\vec{r}) = \int_0^T e^{iE_j t} \Psi(\vec{r}, t) dt \quad (25)$$

Note that at difference with a bound state, the resonance wave function  $\psi^{\text{res}}(\vec{r})$  satisfies the outgoing wave boundary conditions and thus contains the continuum part.

Since the autocorrelation function  $A(t)$  reflects the dynamics of the electronic states of the system populated at  $t = 0$  by projection of the initial wave function  $\Psi_0(\vec{r})$ , the choice of the latter might significantly ease or harm extraction of the resonance characteristics. For this reason, the initial conditions must be carefully chosen and, depending on the states of interest, several propagations might be required to obtain  $\Psi_0(\vec{r})$ . For the study of the anionic resonances at surfaces, the wave function of the  $\pi^*$  LUMO orbital of the gas-phase molecule,  $\Phi_{\text{LUMO}}(\vec{r})$ , provides a good initial condition. Here, the molecular structure is defined by atomic positions  $\{\vec{r}_j^{\text{Ads}}\}$ . Because the direct diagonalization of the FGH is impossible,  $\Phi_{\text{LUMO}}(\vec{r})$  is calculated with WPP for the free-standing molecule following the iterative procedure

$$\psi_{f+1}(\vec{r}) = \int_0^T e^{iE_f t} e^{-\eta t} \Psi_f(\vec{r}, t) dt \quad (26)$$

Here,  $f$  provides the order of approximation,  $\Psi_f(\vec{r}, t)$  is the time-dependent solution of the Schrödinger equation obtained with initial state  $\psi_f(\vec{r})$  (order  $f$  approximation to  $\Phi_{\text{LUMO}}(\vec{r})$ ). The

final propagation time  $T$  and the attenuation  $\eta \simeq 4/T$  are determined by the energy difference  $\Delta\Omega$  between the sought quasistationary state and next in energy state emerging in the fit of the autocorrelation function (see eq 24). Typically, we use  $T \simeq 10 \times 2\pi/\Delta\Omega$ . Because the  $\pi^*$  orbital at the origin of the sought resonances for the molecules adsorbed at metal surface is antisymmetric with respect to the molecular plane, the iterations are started with an initial function given by the Gaussian centered out of the molecular plane. The energy estimate  $E_1$  is obtained from the energy of the LUMO  $\pi^*$  orbital calculated with Abinit for the  $\{\vec{r}_j^{\text{Ads}}\}$  molecular structure. At the following steps, the  $E_f$  energy is obtained from the analysis of the autocorrelation function. Typically, a small number of iteration steps  $f \sim 2, 3$  are enough to obtain good approximation to the eigenstate of the FGH,  $\Phi_{\text{LUMO}}(\vec{r})$ , used as an initial condition for the WPP study of the electronic resonances of the adsorbed molecule. It is worth stressing that eq 26 establishes a general iteration procedure that can be applied to ease the extraction of the energies, widths, and wave functions of the quasistationary states localized on molecules embedded in different environments. In particular, we use it for the surface-adsorbed molecules as shown below.

Figure 4 presents a workflow with the computational strategy proposed in this work, as has been detailed in this section.

### 3. ANION RESONANCES OF VINYL DERIVATIVES ADSORBED ON A CU(100) SURFACE

In this section, we illustrate our approach with the results obtained for the negative ion resonances localized on vinyl derivatives (ACA, ACN, and ACO) adsorbed on a Cu(100).

**3.1. Computational Details.** The calculations have been performed with two different sizes of the uniformly spaced 3D mesh:  $n_x = n_y = n_z = 512$  (regular box) and  $n_x = n_y = 1024$ ,  $n_z = 512$  (large box). While the regular box is used routinely, the large-box-computations are performed for some of the data points to check the convergence of the results. The mesh spacing  $h_x = h_y = h_z = h = 0.169$  a.u. is set equal to the mesh spacing used in the Abinit package. Thus, in the  $z$ -coordinate, perpendicular to the surface the mesh extends within the  $-55$  a.u.  $\leq z \leq 31$  a.u. range as measured from the first layer of the surface atoms (negative  $z$  corresponds to inside the metal, and positive  $z$  corresponds to the vacuum region above the surface). Parallel to the surface, the mesh extends within the  $-43$  a.u.  $\leq x, y \leq 43$  a.u. range for the regular box, and within the  $-86$  a.u.  $\leq x, y \leq 86$  a.u. range for the large box. The propagation time step  $dt = 0.018$  a.u. is used. With the present



choice of  $h$  and  $dt$ , for the free-standing molecule, the KS energies of molecular orbitals obtained using WPP converge with an accuracy of at least 0.1 meV. Simultaneously, the difference between the WPP results and the KS energies of molecular orbitals obtained from the quantum chemistry code (Abinit) is also less than 0.1 meV. Using these values of  $h$  and  $dt$  also provides accurate results for the widths of the resonances at a reasonable computational cost. The absorbing potential set at the boundaries of the mesh is defined using eq 20 with:  $\lambda_- = \lambda_+ = \lambda = 2 \times 10^{-4}$  a.u.;  $x_- = y_- = -23$  a.u. and  $x_+ = y_+ = 23$  a.u. for the regular computation box; and  $x_- = y_- = -46$  a.u. and  $x_+ = y_+ = 46$  a.u. for the large computation box. In both cases  $z_- = -30$  a.u. and  $z_+ = 28$  a.u. is used. Note that because the molecule-localized resonance is located at negative energies with respect to the vacuum level, and because it decays by electron emission inside metal, the calculation can be done without absorber at positive  $z$  without altering the results. Table 1 summarizes the computational details of the WPP simulations.

**Table 1. Summary of the Computational Details in the WPP Simulations<sup>a</sup>**

Time Step $dt = 0.018$ a.u.	
Regular box	Large box
Mesh	
$h_x = h_y = h_z = 0.169$ a.u.	$h_x = h_y = h_z = 0.169$ a.u.
$n_x = n_y = n_z = 512$	$n_x = n_y = 1024, n_z = 512$
$-43$ a.u. $\leq x, y \leq 43$ a.u.	$-86$ a.u. $\leq x, y \leq 86$ a.u.
$-55$ a.u. $\leq z \leq 31$ a.u.	$-55$ a.u. $\leq z \leq 31$ a.u.
Absorbing Potential	
$x_- = y_- = -23$ a.u.	$x_- = y_- = -46$ a.u.
$x_+ = y_+ = 23$ a.u.	$x_+ = y_+ = 46$ a.u.
$z_- = -30$ a.u. $z_+ = 28$ a.u.	$z_- = -30$ a.u. $z_+ = 28$ a.u.
$\lambda_- = \lambda_+ = 2 \times 10^{-4}$ a.u.	$\lambda_- = \lambda_+ = 2 \times 10^{-4}$ a.u.

<sup>a</sup>Within these values, a typical WPP run requires  $\sim 1000$  h of cpu time and  $\sim 50$  Gb of memory. The code has been parallelized and we have checked that up to  $\sim 32$  proc scales linearly.

For the vinyl derivatives adsorbed on the Cu(100) surface, the adsorption geometries have been taken from the most stable structures reported in ref 63. The optimization of the geometry was carried out using the optPBE functional,<sup>107–110</sup> PAW pseudopotentials to describe the electron–ion interactions, and a plane-wave basis set with a kinetic energy cutoff of 750 eV. We used a periodic supercell with a metal slab made by a four-layer ( $5 \times 5$ ), the adsorbed molecule, and a vacuum distance of  $\sim 20$  Å. The Brillouin zone was described with a single  $1 \times 1 \times 1$  point using a  $\Gamma$ -centered Monkhorst–Pack scheme. These calculations were performed with the VASP code.<sup>85–87</sup> See ref 63 for further details. Using these geometries, potentials for the WPP were obtained from the Abinit package<sup>81</sup> calculations, taking advantage of the periodic boundary conditions in order to have a correct description of the metal surface. The interaction between ions and electrons has been described with norm-conserving pseudopotentials.<sup>83</sup> Plane waves up to a kinetic energy of 32 atomic units were used to describe the electron density. Electronic energy was converged until an energy difference of  $10^{-9}$  a.u. was reached. The  $\Gamma$  point was used to sample the reciprocal space. Because, according to the Koopmans' theorem, the LUMO states accommodate an extra electron in molecular anion, we apply

the correction given by eq 11. The molecular affinities in the gas phase necessary to determine the  $U$ -parameter were obtained using the Gaussian09<sup>84</sup> package, by performing single-point calculations at the CCSD/cc-pVTZ level of theory. The same atomic arrangement as in the adsorbed molecule was considered. Because for the free-standing ACA, ACN, and ACO molecules the molecular anions are unbound ( $E_a > 0$ ), special care is taken in order to avoid other states (as Rydberg states), which could appear at lower energies, especially if a large basis set with diffuse functions is used. The resulting energy shift  $U$  values are 3.539, 3.652, and 3.728 eV for ACA, ACN, and ACO, respectively.

**3.2. Results and Discussion.** With initial conditions given by the wave function  $\Phi_{\text{LUMO}}(\vec{r})$  of the  $\pi^*$  molecular orbital obtained from the gas-phase WPP calculations, we carried out the WPP studies of the dynamics of an electron active in RCT between an adsorbed molecule and a metal surface. As follows from our results presented below, the decay of the anion population by the transfer of an extra electron into the metal surface is very fast. In this situation, the quasistationary molecular states appear as broad resonances in pDOS,  $n(E)$ , (see Figure 5), making difficult extraction of their energies and

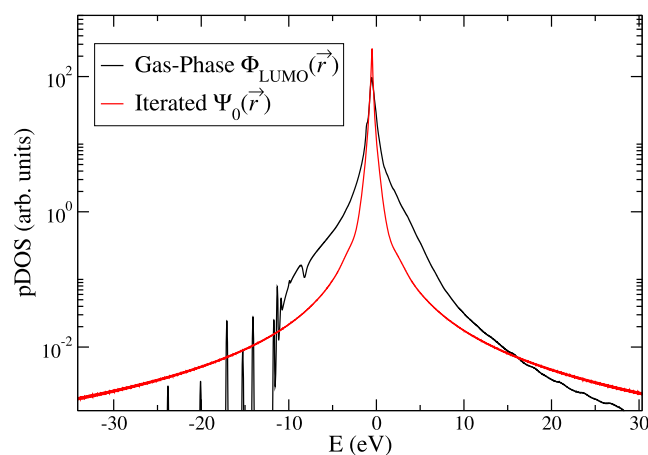


**Figure 5.** ACA molecule adsorbed on the Cu(100) surface. The pDOS obtained in WPP calculations via Fourier transform of the autocorrelation function. Black line: results obtained using the gas-phase LUMO orbital as an initial state for the WPP, red line: results obtained with an initial state of the time propagation extracted from the iterative procedure and approaching the wave function of the anion resonance.

lifetimes. In order to improve the extraction of the resonance parameters, consecutive propagations defined by the iterative procedure given by eq 26 are often required for the adsorbed molecule. The iteration is started with  $\Phi_{\text{LUMO}}(\vec{r})$  allowing estimating the energy  $E_{f=1}^{\text{res}}$  of the quasistationary state. Then, we rerun the WPP with initial state  $\Phi_{\text{LUMO}}(\vec{r})$ , and we extract the resonance energy  $E_{f=1}^{\text{res}}$ . This allows launching the iterations. We repeat the iteration cycles till the pDOS energy spectrum featuring a single peak is retrieved, as shown in Figure 5. Using this iterative procedure, we progressively increase the contribution of the quasistationary state in the initial wave function  $\Psi_0(\vec{r})$ , which eases the extraction of the energy and the decay rate of the molecular localized resonance.

We illustrate the performance of the iterative procedure with an example of the ACA molecule adsorbed on Cu(100). The two consecutive time-propagations are applied. First one is



performed using the gas-phase LUMO orbital as an initial state, and provides an initial state for the second time propagation. In Figure 5, we show the pDOS calculated using different initial states. If the gas-phase LUMO orbital  $\Phi_{\text{LUMO}}(\vec{r})$  is used as an initial state (black line), along with the main peak with maximum at  $E_{\pi^*} = -0.53$  eV and corresponding to the sought quasistationary state, the pDOS shows a reach pattern. Indeed, while  $\Phi_{\text{LUMO}}(\vec{r})$  is the eigenstate of the FGH for the free standing molecule, this is not the case in front of the surface so that pDOS reflects contribution of different eigenstates of the FGH of the compound molecule + surface system populated by the projection on the initial state. Thus, a broad feature extending from approx. -12 eV [valence band bottom of model Cu(100)] to large positive energies is associated with continuum of metal and vacuum electronic states. The structures at high binding energies below the main resonance reflect contributions of various molecular orbitals different from the LUMO. The associated electronic states are stationary when located below the metal band bottom leading to the sharp peaks in pDOS with the width resulting solely from the finite propagation time. Within the energy range of the metal continuum, molecular orbitals are broadened into resonances albeit with their widths essentially smaller than that of the loosely bound LUMO. In sheer contrast with the previous results, the pDOS obtained in the propagation with  $\Psi_0(\vec{r})$  (red line in Figure 5), computed as result of two iterations, features a single Lorentzian peak corresponding to the quasistationary state originating from the LUMO molecular orbital hybridized with the metal surface. Thus, the iterative procedure allows the choice of the initial condition approaching the quasistationary molecule-localized state.

The structure of pDOS characterized by a single resonance or many populated states obviously reflects the time dependence of the autocorrelation function,  $A(t)$ . Both are linked via the Fourier transform. This is illustrated in Figure 6 where we show the time evolution of the population of the initial state,  $|A(t)|^2$ . If only the decaying quasistationary state is populated

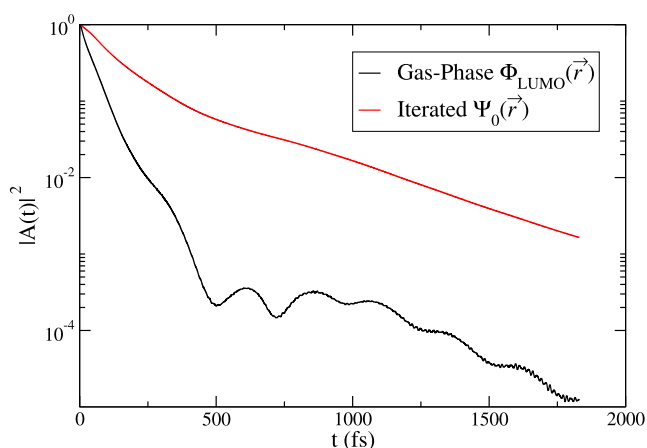


**Figure 6.** ACA molecule adsorbed on the Cu(100) surface. Survival probability of the initial state given by the squared modulus of the autocorrelation function. The WPP is performed using different initial wave functions. Black line: results obtained using the gas-phase LUMO orbital as an initial state for the WPP, red line: results obtained with an initial state of the time propagation extracted from the iterative procedure and approaching the wave function of the anion resonance.

by the choice of initial conditions, one would expect an exponential decay of the population of the initial state. This is observed with initial state  $\Psi_0(\vec{r})$ , obtained from the iterative procedure and approaching the wave function of the quasistationary state (red curve in Figure 6). At variance, using the gas-phase orbital  $\Phi_{\text{LUMO}}(\vec{r})$  as an initial state for the time propagation (black curve in Figure 6) leads to the strong population of metal and vacuum continuum states within a broad energy range. In turn, this results in the fast drop of the initial state population at short propagation times. At longer propagation times, we retrieve an exponential decay of the quasistationary state, with some oscillations. This oscillating pattern is the direct consequence of the interference between different molecular states populated by the choice of initial conditions. In particular, the contribution of bound molecular orbitals below the bottom of metal continuum does not decay in time.

Energies, RCT decay rates (or resonance widths) and lifetimes of the molecular anion resonances computed with WPP are shown in Table 2. The ACA, ACN, and ACO molecules adsorbed on the Cu(100) surface are studied using regular and large spatial extension of the computational mesh. Both sizes of the simulation mesh provide results with differences lower than 0.1 fs in lifetimes and 0.03 eV in resonance energies (which represent less than 5% in all the cases). For the sake of computational efficiency, we then used the regular mesh to describe the energy and the decay dynamics of the molecular induced resonances at surfaces. For all three studied vinyl derivatives, the surface strongly stabilizes the extra electron around the molecule: the obtained energies for the anionic states are negative (i.e., below the vacuum level), whereas in the gas phase, the molecular anions are unbound. Thus, in difference to the gas-phase situation, the molecular anion cannot decay by electron emission into the vacuum. The only possible decay channel is the RCT into the metal, which is allowed because the three anionic resonances have energies above the Fermi level of the surface.

It follows from our results that the RCT is an extremely efficient process and an electron initially localized on the molecule quickly escapes from the molecule potential well into the metal. As we have previously shown,<sup>63,64</sup> the orbitals of the vinyl derivatives (both occupied and unoccupied) are mixed with the metal. The present study confirms this strong coupling, similar for the three studied anions and leading to extremely short lifetimes (below 2 fs) of the molecule-localized resonances of the  $\pi^*$  character. As shown in ref 63, ACN and ACO molecules adsorb in an almost parallel orientation with respect to the metal surface. However, the  $\text{NH}_2$  group of the ACA is oriented toward the vacuum. Then, the LUMO orbital underlying the  $\pi^*$  resonance is less coupled with continuum of metal states, which explains its slightly larger lifetime.

The electron densities of the quasistationary molecular  $\pi^*$  anion states associated with the energies in Table 2 are shown in Figure 7 for the three vinyl-derivatives adsorbed on Cu(100). They are given by the modulus square of the resonant wave-functions  $|\psi_{\pi^*}^{\text{res}}(\vec{r})|^2$  calculated using eq 25. The initial conditions for the WPP are obtained using the iterative procedure given by eq 26. In the three cases,  $|\psi_{\pi^*}^{\text{res}}(\vec{r})|^2$  is characterized by the hybridization between the molecular LUMO orbital and valence band states of the metal: part of the density is localized on the molecule and the rest is spread in a decaying tail inside the metal. The density localized in the organic part retrieves the lobes as in the  $\pi^*$  molecular orbital in

**Table 2.** Energy,  $E_{\pi^*}$ , RCT Decay Rates (Resonance Widths),  $\Gamma$ , and Lifetimes,  $\tau$ , of the Molecular Anion Resonances Computed with WPP for ACA, ACN, and ACO Molecules Adsorbed on the Cu(100) Surface<sup>a</sup>

	regular box			large box		
	ACA	ACN	ACO	ACA	ACN	ACO
$E_{\pi^*}$	−0.580	−0.475	−0.655	−0.582	−0.466	−0.679
$\Gamma$ (eV)	0.41	0.63	0.59	0.42	0.65	0.59
$\tau$ (fs)	1.61	1.04	1.12	1.53	1.01	1.12

<sup>a</sup>The calculations are performed using the regular and large spatial extension of the 3D computational mesh.

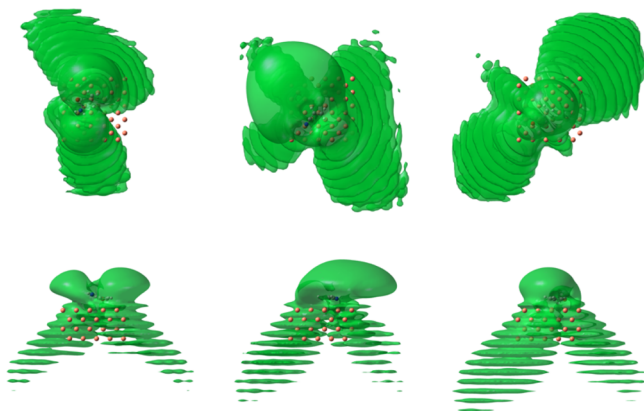


**Figure 7.** Electron densities (isovalue = 0.0025 a.u.) associated with the resonant wavefunctions of the molecular anions of the vinyl derivatives on Cu(100). Top and lateral views are shown for ACA (left), ACN (center), and ACO (right). Color code for the atoms: Cu—orange, C—gray, H—white, N—blue, and O—red.

the gas phase. The decaying tail inside the metal corresponds to the flux of electrons escaping from the decaying quasistationary molecule-localized state into the metal continuum. It presents oscillations because of the metal atomic layers. In addition, the flux of electrons outgoing from the molecule into the metal shows a well pronounced directionality. Thus, electrons escape from the molecule not along the direction perpendicular to the surface plane, which is a shortest path to the metal, and intuitively, the easiest direction of an electron transfer. In contrast to this simple minded picture, the flux of escaping electrons is oriented at some angle with respect to the surface normal.

This effect has been thoroughly studied for the case of adatoms.<sup>13,54</sup> It is a direct consequence of the presence of the projected band gap ( $X$ -gap) of the Cu(100) surface as explained in Figure 8 where we show the energy dispersion of the electronic states relevant for the RCT between the molecule and the metal. Because of the successive reflections by the atomic planes inside Cu(100), the electron propagation in the direction perpendicular to the surface is impossible within the energy range between −3.02 and +3.08 eV with respect to the vacuum level. This energy range is called the projected band gap and it is well captured with model potential for the electron–Cu(100) interaction  $V_{\text{Met}}^{\text{model}}$  proposed in ref 103 and used in our study. Potential  $V_{\text{Met}}^{\text{model}}$  depends only on the electron coordinate perpendicular to the surface, and the free-electron motion parallel to the surface is assumed leading to the energy dispersion of the metal continuum states given using

$$E = \frac{k_{\parallel}^2}{2m^*} + E_z \quad (27)$$

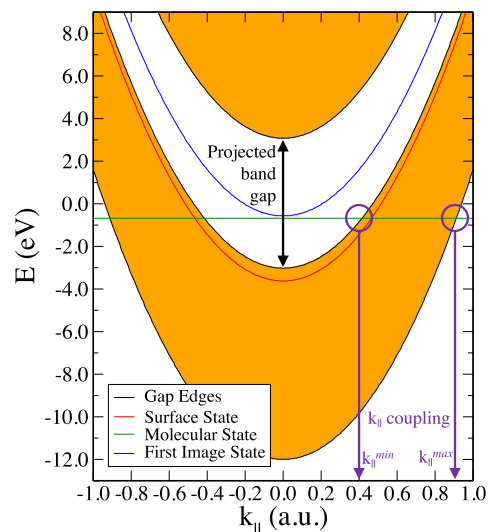


**Figure 8.** Energies of the electronic states relevant for the RCT between molecular anion and metal for the vinyl derivatives adsorbed on Cu(100) surface. The energies measured with respect to the vacuum level are shown as function of the electron momentum parallel to the surface,  $k_{\parallel}$ . The Cu(100) metal is represented with model potential<sup>103</sup> so that the metallic states are characterized by the free electron energy dispersion  $k_{\parallel}^2/2$ . The continuum of the electronic states of the metal is shown with hatched areas separated by the projected band gap. The nondispersing molecule-localized quasistationary state is shown with a horizontal green line. The metal continuum states characterized by  $k_{\parallel}^{\text{min}} \leq k_{\parallel} \leq k_{\parallel}^{\text{max}}$  are in energy resonance with molecular localized states. For the sake of completeness, we also show the surface-localized states of the pristine surface:<sup>103</sup> the surface state resonance and the  $n = 1$  image potential state.

where  $m^*$  is the effective electron mass (1 in the present case),  $\vec{k}_{\parallel} = (k_x, k_y)$  is an electron momentum parallel to the surface, and  $E_z$  describes the electronic structure at the  $\bar{\Gamma}$  point ( $k_x = k_y = 0$ ) corresponding to electron motion in the direction perpendicular to the Cu(100) surface. The molecule-localized quasistationary state at the energy  $E_{\pi^*}$  is nondispersive and it is shown with a horizontal line in Figure 8. Obviously, only the metal continuum states with electron momentum  $k_{\parallel}^{\text{min}} \leq k_{\parallel} \leq k_{\parallel}^{\text{max}}$  are energetically available for the decay of the molecular  $\pi^*$  resonance. Here,  $k_{\parallel}^{\text{min}} \simeq 0.4$  a.u., and  $k_{\parallel}^{\text{max}} \simeq 0.9$  a.u. can be obtained from

$$\begin{aligned} k_{\parallel}^{\text{min}} &= \sqrt{2m^*(E_{\pi^*} - E_{\text{GB}})}, \\ k_{\parallel}^{\text{max}} &= \sqrt{2m^*(E_{\pi^*} - E_{\text{VB}})} \end{aligned} \quad (28)$$

where  $E_{\text{GB}}$  is the energy of the bottom of the projected band gap (−3.02 eV) at  $\bar{\Gamma}$ , and  $E_{\text{VB}}$  is the energy of the bottom of the valence band continuum (−12 eV) at  $\bar{\Gamma}$ . As a result of the projected band structure of the substrate, the flux of the

electrons propagating into the metal bulk is concentrated within a given  $k_{\parallel}$  range, and appears in Figure 7 within at finite angles with respect to the surface normal.

At this point, it is interesting to compare the earlier reported results for the alkali adatoms and the present results for adsorbed molecules. As we demonstrated in Figure 8, the projected band gap blocks the resonant (energy-conserving) electron transfer from the adsorbate into the substrate along the “easiest” direction of the surface normal. For the alkali adsorbate-localized electronic resonances, the long lifetimes ( $\approx 6$  fs for Cs/Cu(100)) have been consequently measured and calculated.<sup>13,54,111</sup> The anion molecular resonances studied here reveal much shorter lifetimes, which can be associated with less-efficient stabilization by the projected band gap. Indeed, as demonstrated for the alkali adatoms, their high polarizability plays a crucial role. It leads to the shift of the electron density of the adsorbate-localized state away from the surface, which enhances the projected band gap effect.<sup>111</sup> The vinyl derivatives studied here lay flat at the surface. The polarizability in the direction perpendicular to the surface is small, and the coupling with the substrate is large resulting in short lifetimes despite the projected band gap is present for the Cu(100) substrate. This explanation is also supported by the WPP calculations for the  $H^{-}$  ion resonance, where similar decay rates (of the order of a fraction of eV) have been reported close to the metal surface in the absorption region.<sup>112</sup> Note also that because in the present situation, the resonant electron transfer leads to a large decay rate of the molecule-localized resonance, the many-body contribution can be neglected.<sup>111</sup> The many-body effects, associated with inelastic scattering events between an active electron and electrons from the metal valence band, typically change the decay rate by  $\approx 20$  meV. When needed, the inelastic electron–electron scattering inside the metal substrate can be accounted for within our method by using a non-Hermitian (absorbing) potential.<sup>113,114</sup>

Another important difference between the present results and earlier calculations for atomic adsorbates consists in the azimuthal anisotropy of the decay as calculated here. While the energy resonance conditions are isotropic regarding the final electron momentum parallel to the surface with no preferential direction, the results in Figure 7 evidence that the intensity of the outgoing electron flux has no axial symmetry. It depends not only on the polar angle  $\theta$  with respect to the surface normal, but also on the azimuthal angle  $\phi$  measured in the plane parallel to the surface between the  $\vec{k}_{\parallel}$  and the  $x$ -axis directed along the  $C_1$ – $C_2$  bond. The orientation of the decay along the well-defined directions of the  $\vec{k}_{\parallel}$ , seen in Figure 7 for vinyl derivatives arises from the properties of the molecular LUMO orbital of  $\pi^*$  character, and it is in sheer contrast with the findings reported so far for adatoms.<sup>13,54</sup>

In order to understand the  $\phi$ -dependence of the anion decay into the metal, let us recall the Bardeen transfer Hamiltonian theory<sup>115–117</sup> routinely applied to explain the STM images or to address an electron transfer in heterostructures. Within the transfer Hamiltonian theory, the decay rate of the molecule in front of the surface is given using the golden rule equation<sup>118</sup>

$$\Gamma = 2\pi \sum_{\vec{k}_{\parallel}, E_z} |M_{\vec{k}_{\parallel}, E_z}|^2 \quad (29)$$

where  $M_{\vec{k}_{\parallel}, E_z}$  are the transition matrix elements between the localized molecular state  $\Phi_{\text{LUMO}}(\vec{r})$  of the  $\pi^*$  character and the metal states  $\psi_{\vec{k}_{\parallel}, E_z}(\vec{r})$

$$M_{\vec{k}_{\parallel}, E_z} = \frac{1}{2} \int dx \int dy \left[ \psi_{\vec{k}_{\parallel}, E_z}(\vec{r}) \frac{\partial}{\partial z} \Phi_{\text{LUMO}}(\vec{r})^* - \Phi_{\text{LUMO}}(\vec{r})^* \frac{\partial}{\partial z} \psi_{\vec{k}_{\parallel}, E_z}(\vec{r}) \right] \quad (30)$$

The integration runs over the surface parallel to the metal and located at any  $z$  position within the tunneling barrier. Obviously, the  $\vec{k}_{\parallel}$  structure of the transition matrix elements defining the electron flux in different  $\vec{k}_{\parallel}$  decay channels reflects the decomposition of the molecular orbital on the basis of plane waves parallel to the surface. One remark is in order, however, regarding the character of the RCT in the present case. The analysis of the total potential of the system shows that an electron is transferred between the metal and the molecule potential wells via the classically allowed over the barrier transition. Thus, albeit it sheds light on the observed trends, the transfer Hamiltonian formalism should be considered here with care.

In order to verify the validity of the qualitative conclusions drawn from eq 30, we have performed a plane wave decomposition of the resonance wave function  $\psi_{\pi^*}^{\text{res}}(\vec{r})$  for the fixed position of the analysis plane  $z = z_0$ . In practice, we computed the quantity

$$C(k_{\parallel}, \phi, z_0) = \int dx \int dy \psi_{\pi^*}^{\text{res}}(\vec{r}) e^{-ik_{\parallel} \cos(\phi)x} e^{-ik_{\parallel} \sin(\phi)y} \quad (31)$$

where the components of the parallel momentum are given by  $k_x = k_{\parallel} \cos(\phi)$  and  $k_y = k_{\parallel} \sin(\phi)$ . From the energy conservation conditions, only the  $k_{\parallel}^{\text{min}} \leq k_{\parallel} \leq k_{\parallel}^{\text{max}}$  range has been considered. For  $z_0$  set in the asymptotic region inside the metal, the molecule-induced potential is screened. Equation 31 corresponds then to the final state analysis and provides the outgoing wave packet decomposition in the basis of the eigenstates of the metal Hamiltonian,  $\psi_{\vec{k}_{\parallel}, E_z}(x, y, z)|_{z=z_0} = e^{ik_{\parallel} \cos(\phi)x} e^{ik_{\parallel} \sin(\phi)y} \chi^+(E_z, z)|_{z=z_0}$ , where the outgoing Bloch wave  $\chi^+(E_z, z)$  is defined by its energy  $E_z = E_{\pi^*} - k_{\parallel}^2/2m^*$ . In particular,  $|C(k_{\parallel}, \phi, z_0)|^2$  calculated in the asymptotic region is proportional to the probability of the RCT from the molecule to the metal continuum state  $\psi_{\vec{k}_{\parallel}, E_z}$ .

The 2D maps of the  $\vec{k}_{\parallel}$  decomposition,  $|C(k_{\parallel}, \phi, z_0)|^2$ , are shown in Figure 9 for ACA, ACN, and ACO molecules interacting with the Cu(100) surface. Three different positions of the analysis plane have been considered:  $z_0 = 2$  a.u. between the molecule and the metal,  $z_0 = 0$  corresponding to the first metal surface layer, and  $z_0 = -6$  a.u. (negative  $z$  corresponds to the metal bulk). While  $z_0 = 2$  a.u. is not located in the asymptotic region, for  $z_0 = 0$  and  $z_0 = -6$  a.u. inside the metal, a similar pattern is observed indicating convergence toward the asymptotic solution. Here, the outgoing wave imprints the gross features of the  $\vec{k}_{\parallel}$  decomposition of the molecular LUMO orbital, which is behind the resonance. For the free-standing ACO and ACN molecules,  $\Phi_{\text{LUMO}}(\vec{r})$  is illustrated in Figure 10. Using this figure, the maxima in the angular dependence of  $|C(k_{\parallel}, \phi, z_0)|$  observed for ACO at  $\phi = 45^\circ$  and  $\phi = 135^\circ$  can be identified as resulting from the overall orientation of the  $\Phi_{\text{LUMO}}(\vec{r})$  with respect to the  $C_1$ – $C_2$  bond (set as  $x$ -axis). Similar explanation holds for the angular dependence of the final state occupation amplitudes in the case of ACA. The structure of the LUMO orbital of ACN cannot be characterized by the overall linear alignment, but rather



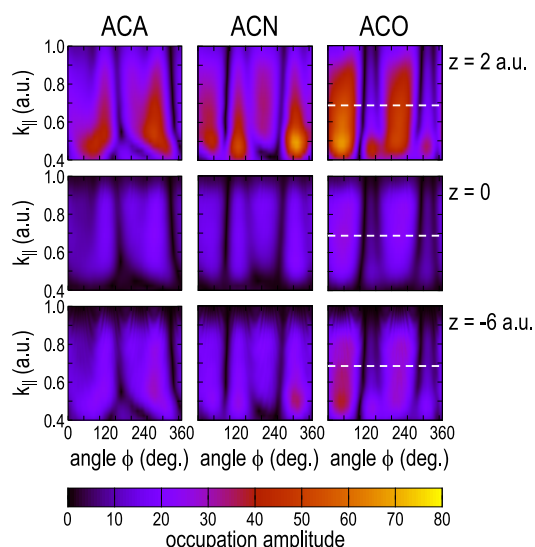


**Figure 9.** 2D maps of the  $\vec{k}_{\parallel}$  decomposition  $|C(k_{\parallel}, \phi, z_0)|^2$ , for the ACA left column, the ACN central column, and the ACO right column. The data are shown as a function of the azimuthal angle,  $\phi$ , and the absolute value of the electron momentum parallel to the surface,  $k_{\parallel}$ . The analysis plane is parallel to the metal surface and located between the molecule and the surface ( $z_0 = 2$  a.u.), upper row, at the first atomic layer of Cu(100) ( $z_0 = 0$ ), central row, and inside the Cu(100) ( $z_0 = -6$  a.u.), lower row. The analysis has been performed for the metal electronic states with  $k_{\parallel}^{\min} \leq k_{\parallel} \leq k_{\parallel}^{\max}$  available for the electron transfer from the molecule localized resonance. The color code is explained with a horizontal color bar. The horizontal dashed line indicates the characteristic structure wave vector of the ACO molecule. For further details, see the text.

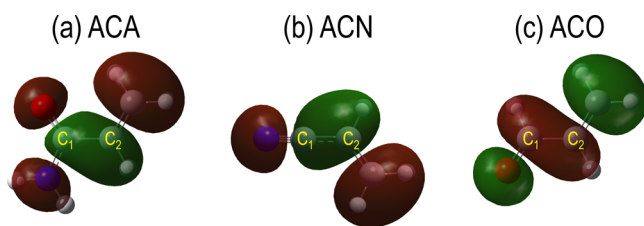


**Figure 10.** LUMO orbital of (a) ACA, (b) ACN, and (c) ACO molecules in the gas phase. Red and green denote different phases. An isovalue for the surface of 0.02 a.u. has been used.

features two preferential directions rotated by  $\phi = 120^\circ$  in the  $(x, y)$ -plane. Consequently, four maxima are observed in the angular dependence of the final state population amplitudes in Figure 9. Interestingly,  $\Phi_{\text{LUMO}}(\vec{r})$  of ACO (Figure 10) features a 4.6 a.u. spacing between the nodes in the  $\phi = 45^\circ$  direction leading to the characteristic molecular structure wave vector  $k_{\parallel}^{\text{Mol}} = 0.68$  a.u. It falls within the range of the wave vectors in Figure 9 and it is indicated with a dashed line.

Finally, the remark is in order concerning the essential role of the energy correction as implemented in the nonlocal potential given by eq 11. Without the energy correction, the  $\pi^*$ -resonance of the molecular anion shifts to much lower energy (e.g.  $E_{\pi^*} \sim -4$  eV for the ACO molecule) below the projected band gap of the Cu(100) surface. The RCT along the easiest direction perpendicular to the surface becomes possible. This is possible because the metal continuum states with  $0 \leq k_{\parallel} \leq k_{\parallel}^{\max}$  are now available for the RCT provided that their energy  $E_z = E_{\pi^*} - k_{\parallel}^2/2m^*$ . Not only this leads to a faster decay rate ( $\Gamma = 0.65$  eV) and the corresponding shortening of

the lifetime of the molecule-localized state ( $\tau = 1$  fs) but also the momentum distribution of the hot electrons injected into the metal is completely modified.

#### 4. CONCLUSIONS

We have presented a method for studying ultrafast electron dynamics in complex molecular systems characterized by the discrete state-continuum interaction. The methodology grounds on a real-time solution of the TDSE where the wave function of the active electron is represented on a spatial mesh of points and the WPP technique is applied. One of the most important advantages of our approach is that it incorporates the versatile character of the WPP on real space grids in describing the propagating continuum states, together with the realistic electronic structure of the adsorbed molecule. The electron–molecule interaction potential is obtained from ground state DFT simulations and it allows the explicit inclusion of the inner shell electrons. While leading to the sharp and strong potentials, this choice has a twofold advantage. First, it guarantees that the KS orbitals representing the bound molecular states are strictly the same at the ab initio and WPP levels, which is important as far as the correct choice of initial state is concerned; second, the scattering of the continuum electrons by the molecule can be addressed up to relatively high electron energies relevant, for example, for studies of attosecond photoemission delays<sup>16,65,119,120</sup> or electron rescattering in the optical field emission.<sup>15,66–68</sup> Thus, the technique presented here benefits from the state-of-the-art ab initio description of the molecular system and, simultaneously, from the easiness to account for the continuum states within the WPP.

We illustrate our method with the case study of RCT processes between the anion states of organic molecules and the metal surfaces. For the three vinyl derivatives ACA, ACN, and ACO, adsorbed on a Cu(100) surface, we report the detailed characterization of molecular localized anion resonance, decaying via electron escape into the continuum of the electronic states of the metal. The energy, RCT rate, resonant wavefunction, and decay channels are calculated with WPP using analysis tools detailed in this work. We introduce a strategy to compute the potential probed by an active electron in the RCT, for the molecules adsorbed at metal surfaces. To this end, we combine (i) a model potential to describe the Cu(100) metal continuum, (ii) DFT simulations of molecular adsorption to account for the molecular structure and charge transfer effects between the molecule and the surface, and (iii) high level ab initio coupled cluster calculations to determine the molecular electron affinity. We have found an ultrafast decay of the molecular localized anion resonances where an electron escapes from the molecule into the metal on a time scale below 2 fs. While this result resembles to that observed earlier with adatoms,<sup>13,54</sup> the molecular nature of the adsorbate leads to the new effects. Namely, the spatial distribution of the hot electrons, injected into the metal by the decaying molecules, reveals a highly marked directionality, which can be rooted back to the structure of the LUMO  $\pi^*$  orbital underlying the anion resonance.

While illustrated here with an example of the lifetimes of resonances in adsorbed molecules at metal surfaces, our approach can deal with general problems of electron escape from molecular systems into a continuum, including the case of photoionization, triggered by short and intense laser pulses, process of relevance for attosecond science.



## ■ AUTHOR INFORMATION

## Corresponding Author

Sergio Díaz-Tendero – Departamento de Química, Módulo 13, Condensed Matter Physics Center (IFIMAC), and Institute for Advanced Research in Chemical Science (IAdChem), Universidad Autónoma de Madrid, Madrid 28049, Spain; [orcid.org/0000-0001-6253-6343](https://orcid.org/0000-0001-6253-6343); Email: [sergio.diaztendero@uam.es](mailto:sergio.diaztendero@uam.es)

## Authors

Fernando Aguilar-Galindo – Departamento de Química, Módulo 13, Universidad Autónoma de Madrid, Madrid 28049, Spain; Donostia International Physics Center (DIPC), Donostia-San Sebastián E-20018, Spain; [orcid.org/0000-0003-2751-5592](https://orcid.org/0000-0003-2751-5592)

Andrey G. Borisov – Institut des Sciences Moléculaires d'Orsay, UMR 8214, CNRS, Université Paris-Saclay, Orsay 91405, France; [orcid.org/0000-0003-0819-5028](https://orcid.org/0000-0003-0819-5028)

Complete contact information is available at:  
<https://pubs.acs.org/10.1021/acs.jctc.0c01031>

## Notes

The authors declare no competing financial interest.

## ■ ACKNOWLEDGMENTS

We acknowledge the generous allocation of computer time at the Centro de Computación Científica at the Universidad Autónoma de Madrid (CCC-UAM) and the Red Española de Supercomputación (RES). This work was partially supported by the MICINN—Spanish Ministry of Science and Innovation—projects CTQ2016-76061-P and PID2019-110091GB-I00 and the “María de Maeztu” (CEX2018-000805-M) Program for Centers of Excellence in R&D. F.A.-G. gratefully acknowledges the hospitality extended to him during his stay at the Institut des Sciences Moléculaires d'Orsay (France).

## ■ REFERENCES

- (1) Seideman, T.; Miller, W. H. Quantum Mechanical Reaction Probabilities Via a Discrete Variable Representation—Absorbing Boundary Condition Green's Function. *J. Chem. Phys.* **1992**, *97*, 2499–2514.
- (2) Jolicard, G.; Leforestier, C.; Austin, E. J. Resonance States Using the Optical Potential Model. Study of Feshbach Resonances and Broad Shape Resonances. *J. Chem. Phys.* **1988**, *88*, 1026–1031.
- (3) Rom, N.; Ryabov, V.; Moiseyev, N. Cumulative Reaction Probability by the Complex Coordinate Scattering Theory. *J. Chem. Phys.* **1993**, *98*, 6327–6331.
- (4) Moiseyev, N. Quantum Theory of Resonances: Calculating Energies, Widths and Cross-Sections by Complex Scaling. *Phys. Rep.* **1998**, *302*, 212–293.
- (5) Mandelshtam, V. A.; Taylor, H. S. Spectral Analysis of Time Correlation Function for a Dissipative Dynamical System Using Filter Diagonalization: Application to Calculation of Unimolecular Decay Rates. *Phys. Rev. Lett.* **1997**, *78*, 3274–3277.
- (6) Leforestier, C.; Bisseling, R. H.; Cerjan, C.; Feit, M. D.; Friesner, R.; Guldberg, A.; Hammerich, A.; Jolicard, G.; Karrlein, W.; Meyer, H.-D.; Lipkin, N.; Roncero, O.; Kosloff, R. A comparison of different propagation schemes for the time dependent Schrödinger equation. *J. Comput. Phys.* **1991**, *94*, 59–80.
- (7) Truong, T. N.; Tanner, J. J.; Bala, P.; McCammon, J. A.; Kouri, D. J.; Lesyng, B.; Hoffman, D. K. A Comparative Study of Time Dependent Quantum Mechanical Wave Packet Evolution Methods. *J. Chem. Phys.* **1992**, *96*, 2077–2084.
- (8) Kosloff, R. Time-Dependent Quantum-Mechanical Methods for Molecular Dynamics. *J. Phys. Chem.* **1988**, *92*, 2087–2100.
- (9) Kosloff, R. Quantum Molecular Dynamics on Grids. *Dynamics of Molecules and Chemical Reactions*; Marcel Dekker, Inc., 1996; pp 185–230.
- (10) Zhang, J. Z. H. *Theory and Application of Quantum Molecular Dynamics*; World Scientific, 1998.
- (11) Kroes, G. Six-Dimensional Quantum Dynamics of Dissociative Chemisorption of H<sub>2</sub> on Metal Surfaces. *Prog. Surf. Sci.* **1999**, *60*, 1–85.
- (12) Beck, M.; Jackle, A.; Worth, G.; Meyer, H.-D. The Multiconfiguration Time-Dependent Hartree (MCTDH) Method: a Highly Efficient Algorithm for Propagating Wavepackets. *Phys. Rep.* **2000**, *324*, 1–105.
- (13) Chulkov, E. V.; Borisov, A. G.; Gauyacq, J. P.; Sánchez-Portal, D.; Silkin, V. M.; Zhukov, V. P.; Echenique, P. M. Electronic Excitations in Metals and at Metal Surfaces. *Chem. Rev.* **2006**, *106*, 4160–4206.
- (14) Sainadh, U. S.; Xu, H.; Wang, X.; Atia-Tul-Noor, A.; Wallace, W. C.; Douguet, N.; Bray, A.; Ivanov, I.; Bartschat, K.; Kheifets, A.; Sang, R. T.; Litvinyuk, I. V. Attosecond Angular Streaking and Tunnelling Time in Atomic Hydrogen. *Nature* **2019**, *568*, 75–77.
- (15) Nisoli, M.; Decleva, P.; Calegari, F.; Palacios, A.; Martín, F. Attosecond Electron Dynamics in Molecules. *Chem. Rev.* **2017**, *117*, 10760–10825.
- (16) Siek, F.; Neb, S.; Bartz, P.; Hensen, M.; Strüber, C.; Fiechter, S.; Torrent-Sucarrat, M.; Silkin, V. M.; Krasovskii, E. E.; Kabachnik, N. M.; Fritzsche, S.; Muiño, R. D.; Echenique, P. M.; Kazansky, A. K.; Müller, N.; Pfeiffer, W.; Heinzmann, U. Angular momentum-induced delays in solid-state photoemission enhanced by intra-atomic interactions. *Science* **2017**, *357*, 1274–1277.
- (17) Saalfrank, P. Quantum Dynamics of Laser- and Field-Induced Desorption of Molecules from Metal Surfaces. *Int. J. Quantum Chem.* **2000**, *80*, 210–219.
- (18) Yang, L.; Epstein, I. R. Chemical Wave Packet Propagation, Reflection, and Spreading. *J. Phys. Chem. A* **2002**, *106*, 11676–11682.
- (19) Johnson, R. E.; Bowman, J. M. In *Encyclopedia of Physical Science and Technology*, 3rd ed.; Meyers, R. A., Ed.; Academic Press: New York, 2003; pp 721–744.
- (20) Meyer, H.-D.; Worth, G. A. Quantum Molecular Dynamics: Propagating Wavepackets and Density Operators Using the Multiconfiguration Time-Dependent Hartree Method. *Theor. Chem. Acc.* **2003**, *109*, 251–267.
- (21) Sielk, J.; von Horsten, H. F.; Krüger, F.; Schneider, R.; Hartke, B. Quantum-Mechanical Wavepacket Propagation in a Sparse, Adaptive Basis of Interpolating Gaussians with Collocation. *Phys. Chem. Chem. Phys.* **2009**, *11*, 463–475.
- (22) Cvitaš, M. T.; Althorpe, S. C. Quantum Wave Packet Method for State-to-State Reactive Scattering Calculations on AB + CD → ABC + D Reactions. *J. Phys. Chem. A* **2009**, *113*, 4557–4569.
- (23) Nyman, G. Computational Methods of Quantum Reaction Dynamics. *Int. J. Quantum Chem.* **2014**, *114*, 1183–1198.
- (24) Grabowski, P. E. A Review of Wave Packet Molecular Dynamics. *Frontiers and Challenges in Warm Dense Matter*; Springer: Cham, 2014; pp 265–282.
- (25) Sun, Z. In *Research Advances in Quantum Dynamics*; Bracken, P., Ed.; IntechOpen: Rijeka, 2016; Chapter 9.
- (26) Baek, K. K. Basics of the Time-Dependent Wave-Packet Propagation for Photodissociations of Polyatomic Systems. *Int. J. Quantum Chem.* **2016**, *116*, 634–643.
- (27) Lounis, B.; Moerner, W. E. Single Photons on Demand from a Single Molecule at Room Temperature. *Nature* **2000**, *407*, 491–493.
- (28) Moerner, W. E. Single-Photon Sources Based on Single Molecules in Solids. *New J. Phys.* **2004**, *6*, 88.
- (29) Merino, P.; Große, C.; Rosławska, A.; Kuhnke, K.; Kern, K. Exciton Dynamics of C60-Based Single-Photon Emitters Explored by Hanbury Brown–Twiss Scanning Tunnelling Microscopy. *Nat. Commun.* **2015**, *6*, 8461.
- (30) Zhang, L.; Yu, Y.-J.; Chen, L.-G.; Luo, Y.; Yang, B.; Kong, F.-F.; Chen, G.; Zhang, Y.; Zhang, Q.; Luo, Y.; Yang, J.-L.; Dong, Z.-C.

Hou, J. G. Electrically Driven Single-Photon Emission from an Isolated Single Molecule. *Nat. Commun.* **2017**, *8*, 580.

(31) Jin, J. M.; Lin, W. F.; Christensen, P. A. The Effects of the Specific Adsorption of Anion on the Reactivity of the Ru(0001) Surface Towards CO Adsorption and Oxidation: in situ FTIRS Studies. *Phys. Chem. Chem. Phys.* **2008**, *10*, 3774–3783.

(32) Busó-Rogero, C.; Grozovski, V.; Vidal-Iglesias, F. J.; Solla-Gullón, J.; Herrero, E.; Feliu, J. M. Surface Structure and Anion Effects in the Oxidation of Ethanol on Platinum Nanoparticles. *J. Mater. Chem. A* **2013**, *1*, 7068–7076.

(33) Petrova, M.; Guigue, M.; Venault, L.; Moisy, P.; Hesemann, P. Anion Selectivity In Ion Exchange Reactions With Surface Functionalized Ionosilicas. *Phys. Chem. Chem. Phys.* **2015**, *17*, 10182–10188.

(34) Mueller, D. N.; Machala, M. L.; Bluhm, H.; Chueh, W. C. Redox Activity of Surface Oxygen Anions in Oxygen-Deficient Perovskite Oxides During Electrochemical Reactions. *Nat. Commun.* **2015**, *6*, 6097.

(35) Álvarez, A.; Borges, M.; Corral-Pérez, J. J.; Olcina, J. G.; Hu, L.; Cornu, D.; Huang, R.; Stoian, D.; Urakawa, A. CO<sub>2</sub> Activation over Catalytic Surfaces. *ChemPhysChem* **2017**, *18*, 3135–3141.

(36) Sheng, H.; Oh, M. H.; Osowiecki, W. T.; Kim, W.; Alivisatos, A. P.; Frei, H. Carbon Dioxide Dimer Radical Anion as Surface Intermediate of Photoinduced CO<sub>2</sub> Reduction at Aqueous Cu and CdSe Nanoparticle Catalysts by Rapid-Scan FT-IR Spectroscopy. *J. Am. Chem. Soc.* **2018**, *140*, 4363–4371.

(37) Maneepong, S.; Wada, S.-I. Stability of Cl<sup>−</sup>NO<sub>3</sub><sup>−</sup>, ClO<sub>4</sub><sup>−</sup>, and SO<sub>4</sub><sup>2−</sup> Surface Complexes at Synthetic Goethite/Aqueous Electrolyte Interfaces. *Soil Sci. Plant Nutr.* **1991**, *37*, 141–150.

(38) Guo, H.; Saalfrank, P.; Seideman, T. Theory of Photoinduced Surface Reactions of Admolecules. *Prog. Surf. Sci.* **1999**, *62*, 239–303.

(39) Saalfrank, P. Quantum Dynamical Approach to Ultrafast Molecular Desorption from Surfaces. *Chem. Rev.* **2006**, *106*, 4116–4159.

(40) Golibrzuch, K.; Bartels, N.; Auerbach, D. J.; Wodtke, A. M. The Dynamics of Molecular Interactions and Chemical Reactions at Metal Surfaces: Testing the Foundations of Theory. *Annu. Rev. Phys. Chem.* **2015**, *66*, 399–425.

(41) Avouris, P.; Persson, B. N. J. Excited States at Metal Surfaces and their Non-Radiative Relaxation. *J. Phys. Chem.* **1984**, *88*, 837–848.

(42) Reecht, G.; Scheurer, F.; Speisser, V.; Dappe, Y. J.; Mathevet, F.; Schull, G. Electroluminescence of a Polythiophene Molecular Wire Suspended between a Metallic Surface and the Tip of a Scanning Tunneling Microscope. *Phys. Rev. Lett.* **2014**, *112*, 047403.

(43) Repp, J.; Meyer, G.; Paavilainen, S.; Olsson, F. E.; Persson, M. Imaging Bond Formation Between a Gold Atom and Pentacene on an Insulating Surface. *Science* **2006**, *312*, 1196–1199.

(44) Soe, W.-H.; Manzano, C.; De Sarkar, A.; Chandrasekhar, N.; Joachim, C. Direct Observation of Molecular Orbitals of Pentacene Physisorbed on Au(111) by Scanning Tunneling Microscope. *Phys. Rev. Lett.* **2009**, *102*, 176102.

(45) Garnica, M.; Stradi, D.; Calleja, F.; Barja, S.; Díaz, C.; Alcamí, M.; Arnau, A.; Vázquez de Parga, A. L.; Martín, F.; Miranda, R. Probing the Site-Dependent Kondo Response of Nanostructured Graphene with Organic Molecules. *Nano Lett.* **2014**, *14*, 4560–4567.

(46) Zhang, Y.; Liao, P.; Kan, J.; Yin, C.; Li, N.; Liu, J.; Chen, Q.; Wang, Y.; Chen, W.; Xu, G. Q.; Jiang, J.; Berndt, R.; Wu, K. Low-Temperature Scanning Tunneling Microscopy Study on the Electronic Properties of a Double-Decker DyPc2 Molecule at the Surface. *Phys. Chem. Chem. Phys.* **2015**, *17*, 27019–27026.

(47) Petek, H.; Weida, M. J.; Nagano, H.; Ogawa, S. Real-Time Observation of Adsorbate Atom Motion Above a Metal Surface. *Science* **2000**, *288*, 1402–1404.

(48) Weinelt, M. Time-Resolved Two-Photon Photoemission From Metal Surfaces. *J. Phys.: Condens. Matter* **2002**, *14*, R1099–R1141.

(49) Zhu, X.-Y. Electron Transfer At Molecule-Metal Interfaces: A Two-Photon Photoemission Study. *Annu. Rev. Phys. Chem.* **2002**, *53*, 221–247.

(50) Gütde, J.; Berthold, W.; Höfer, U. Dynamics of Electronic Transfer Processes at Metal/Insulator Interfaces. *Chem. Rev.* **2006**, *106*, 4261–4280.

(51) Gavnholt, J.; Olsen, T.; Englund, M.; Schiøtz, J.  $\Delta$  self-consistent field method to obtain potential energy surfaces of excited molecules on surfaces. *Phys. Rev. B: Condens. Matter Mater. Phys.* **2008**, *78*, 075441.

(52) Maurer, R. J.; Reuter, K. Bistability Loss as a Key Feature in Azobenzene (Non-)Switching on Metal Surfaces. *Angew. Chem., Int. Ed.* **2012**, *51*, 12009–12011.

(53) Maurer, R. J.; Reuter, K. Excited-state potential-energy surfaces of metal-adsorbed organic molecules from linear expansion  $\Delta$ -self-consistent field density-functional theory ( $\Delta$ SCF-DFT). *J. Chem. Phys.* **2013**, *139*, 014708.

(54) Borisov, A. G.; Gauyacq, J. P.; Kazansky, A. K.; Chulkov, E. V.; Silkin, V. M.; Echenique, P. M. Long-Lived Excited States at Surfaces: Cs/Cu(111) and Cs/Cu(100) Systems. *Phys. Rev. Lett.* **2001**, *86*, 488–491.

(55) Kürpick, P.; Thumm, U.; Wille, U. Resonance Formation of Hydrogenic Levels in Front of Metal Surfaces. *Phys. Rev. A: At., Mol., Opt. Phys.* **1997**, *56*, 543–554.

(56) Martín, F.; Politis, M. F. Multicenter-Gaussian Representation of Resonant Charge Transfer in Atom-Surface Interaction. *Surf. Sci.* **1996**, *356*, 247–256.

(57) Zugarramurdi, A.; Zabala, N.; Silkin, V. M.; Borisov, A. G.; Chulkov, E. V. Lifetimes of Quantum Well States and Resonances in Pb Overlayers on Cu(111). *Phys. Rev. B: Condens. Matter Mater. Phys.* **2009**, *80*, 115425.

(58) Díaz-Tendero, S.; Borisov, A. G.; Gauyacq, J. P. Different Quantization Behaviors of Electrons Confined in Nanostructures at Surfaces. *Phys. Rev. B: Condens. Matter Mater. Phys.* **2007**, *76*, 155428.

(59) Díaz-Tendero, S.; Olsson, F. E.; Borisov, A. G.; Gauyacq, J.-P. Theoretical Study of Electron Confinement in Cu Corrals on a Cu(111) Surface. *Phys. Rev. B: Condens. Matter Mater. Phys.* **2008**, *77*, 205403.

(60) Díaz-Tendero, S.; Foelsch, S.; Olsson, F. E.; Borisov, A. G.; Gauyacq, J.-P. Electron Propagation Along Cu Nanowires Supported on a Cu(111) Surface. *Nano Lett.* **2008**, *8*, 2712–2717.

(61) Díaz-Tendero, S.; Borisov, A. G.; Gauyacq, J.-P. Extraordinary Electron Propagation Length in a Metallic Double Chain Supported on a Metal Surface. *Phys. Rev. Lett.* **2009**, *102*, 166807.

(62) Müller, M.; Sánchez-Portal, D.; Lin, H.; Brivio, G. P.; Selloni, A.; Fratesi, G. Effect of Structural Fluctuations on Elastic Lifetimes of Adsorbate States: Isonicotinic Acid on Rutile(110). *J. Phys. Chem. C* **2018**, *122*, 7575–7585.

(63) Aguilar-Galindo, F.; Díaz-Tendero, S. Theoretical Insights Into Vinyl Derivatives Adsorption on a Cu(100) Surface. *J. Phys. Chem. C* **2018**, *122*, 27301–27313.

(64) Aguilar-Galindo, F.; Díaz-Tendero, S. Outstanding Energy Exchange between Organic Molecules and Metal Surfaces: Decomposition Kinetics of Excited Vinyl Derivatives Driven by the Interaction with a Cu(111) Surface. *J. Phys. Chem. C* **2019**, *123*, 19625–19636.

(65) Biswas, S.; Förg, B.; Ortmann, L.; Schötz, J.; Schweinberger, W.; Zimmermann, T.; Pi, L.; Baykusheva, D.; Masood, H. A.; Lontos, I.; Kamal, A. M.; Kling, N. G.; Alharbi, A. F.; Alharbi, M.; Azzeer, A. M.; Hartmann, G.; Wörner, H. J.; Landsman, A. S.; Kling, M. F. Probing Molecular Environment Through Photoemission Delays. *Nat. Phys.* **2020**, *16*, 778–783.

(66) Meckel, M.; Comtois, D.; Zeidler, D.; Staudte, A.; Pavičić, D.; Bandulet, H. C.; Pépin, H.; Kieffer, J. C.; Dörner, R.; Villeneuve, D. M.; Corkum, P. B. Laser-Induced Electron Tunneling and Diffraction. *Science* **2008**, *320*, 1478–1482.

(67) Lin, C. D.; Le, A.-T.; Chen, Z.; Morishita, T.; Lucchese, R. Strong-field Rescattering Physics—Self-Imaging of a Molecule by its Own Electrons. *J. Phys. B: At., Mol. Opt. Phys.* **2010**, *43*, 122001.

(68) Wolter, B.; Pullen, M. G.; Le, A.-T.; Baudisch, M.; Doblhoff-Dier, K.; Senftleben, A.; Hemmer, M.; Schröter, C. D.; Ullrich, J.; Pfeifer, T.; Moshhammer, R.; Gräfe, S.; Vendrell, O.; Lin, C. D.;



Biegert, J. Ultrafast Electron Diffraction Imaging of Bond Breaking in Di-Ionized Acetylene. *Science* **2016**, *354*, 308–312.

(69) Feit, M. D.; Fleck, J. A.; Steiger, A. Solution of the Schrödinger Equation by a Spectral Method. *J. Comput. Phys.* **1982**, *47*, 412–433.

(70) Kosloff, D.; Kosloff, R. Fourier Method Solution for the Time Dependent Schrödinger Equation as a Tool in Molecular Dynamics. *J. Comput. Phys.* **1983**, *52*, 35–53.

(71) Tal-Ezer, H.; Kosloff, R. An Accurate and Efficient Scheme for Propagating the Time Dependent Schrödinger Equation. *J. Chem. Phys.* **1984**, *81*, 3967–3971.

(72) Park, T. J.; Light, J. C. Unitary Quantum Time Evolution by Iterative Lanczos Reduction. *J. Chem. Phys.* **1986**, *85*, 5870–5876.

(73) Bandrauk, A. D.; Shen, H. Improved Exponential Split Operator Method for Solving the Time-Dependent Schrödinger Equation. *Chem. Phys. Lett.* **1991**, *176*, 428–432.

(74) Huang, Y.; Kouri, D. J.; Hoffman, D. K. General, Energy-Separable Faber Polynomial Representation of Operator Functions: Theory and Application in Quantum Scattering. *J. Chem. Phys.* **1994**, *101*, 10493–10506.

(75) Huisinga, W.; Pesce, L.; Kosloff, R.; Saalfrank, P. Faber and Newton Polynomial Integrators for Open-System Density Matrix Propagation. *J. Chem. Phys.* **1999**, *110*, 5538–5547.

(76) Lin, J. S.; Qteish, A.; Payne, M. C.; Heine, V. Optimized and transferable nonlocal separable ab initio pseudopotentials. *Phys. Rev. B: Condens. Matter Mater. Phys.* **1993**, *47*, 4174–4180.

(77) Gonze, X.; Beuken, J.-M.; Caracas, R.; Detraux, F.; Fuchs, M.; Rignanese, G.-M.; Sindic, L.; Verstraete, M.; Zerah, G.; Jollet, F.; Torrent, M.; Roy, A.; Mikami, M.; Ghosez, P.; Raty, J.-Y.; Allan, D. C. First-Principles Computation of Material Properties: The ABINIT Software Project. *Comput. Mater. Sci.* **2002**, *25*, 478–492.

(78) Gonze, X.; Rignanese, G.-M.; Verstraete, M.; Beuken, J.-M.; Pouillon, Y.; Caracas, R.; Jollet, F.; Torrent, M.; Zerah, G.; Mikami, M.; Ghosez, P.; Veithen, M.; Raty, J.-Y.; Olevano, V.; Bruneval, F.; Reining, L.; Godby, R.; Onida, G.; Hamann, D. R.; Allan, D. C. A Brief Introduction to the ABINIT Software Package. *Z. Kristallogr.—Cryst. Mater.* **2005**, *220*, 558–562.

(79) Feit, M. D.; Fleck, J. A. Solution of the Schrödinger equation by a spectral method II: Vibrational energy levels of triatomic molecules. *J. Chem. Phys.* **1983**, *78*, 301–308.

(80) Gonze, X.; Amadon, B.; Anglade, P.-M.; Beuken, J.-M.; Bottin, F.; Boulanger, P.; Bruneval, F.; Caliste, D.; Caracas, R.; Côté, M.; Deutsch, T.; Genovese, L.; Ghosez, P.; Giantomassi, M.; Goedecker, S.; Hamann, D. R.; Hermet, P.; Jollet, F.; Jomard, G.; Leroux, S.; Mancini, M.; Mazevet, S.; Oliveira, M. J. T.; Onida, G.; Pouillon, Y.; Rangel, T.; Rignanese, G.-M.; Sangalli, D.; Shaltaf, R.; Torrent, M.; Verstraete, M. J.; Zerah, G.; Zwanziger, J. W. ABINIT: First-Principles Approach to Material and Nanosystem Properties. *Comput. Phys. Commun.* **2009**, *180*, 2582–2615.

(81) Gonze, X.; Jollet, F.; Abreu Araujo, F.; Adams, D.; Amadon, B.; Applencourt, T.; Audouze, C.; Beuken, J.-M.; Bieder, J.; Bokhanchuk, A.; Bousquet, E.; Bruneval, F.; Caliste, D.; Côté, M.; Dahm, F.; Da Pieve, F.; Delaveau, M.; Di Gennaro, M.; Dorado, B.; Espejo, C.; Geneste, G.; Genovese, L.; Gerossier, A.; Giantomassi, M.; Gillet, Y.; Hamann, D. R.; He, L.; Jomard, G.; Laflamme Janssen, J.; Le Roux, S.; Levitt, A.; Lherbier, A.; Liu, F.; Lukačević, I.; Martin, A.; Martins, C.; Oliveira, M. J. T.; Poncé, S.; Pouillon, Y.; Rangel, T.; Rignanese, G.-M.; Romero, A. H.; Rousseau, B.; Rubel, O.; Shukri, A. A.; Stankovski, M.; Torrent, M.; Van Setten, M. J.; Van Troeye, B.; Verstraete, M. J.; Waroquiers, D.; Wiktor, J.; Xu, B.; Zhou, A.; Zwanziger, J. W. Recent Developments in the ABINIT Software Package. *Comput. Phys. Commun.* **2016**, *205*, 106–131.

(82) Gonze, X.; Amadon, B.; Antonius, G.; Arnardi, F.; Baguet, L.; Beuken, J.-M.; Bieder, J.; Bottin, F.; Bouchet, J.; Bousquet, E.; Brouwer, N.; Bruneval, F.; Brunin, G.; Cavignac, T.; Charraud, J.-B.; Chen, W.; Côté, M.; Cottenier, S.; Denier, J.; Geneste, G.; Ghosez, P.; Giantomassi, M.; Gillet, Y.; Gingras, O.; Hamann, D. R.; Hautier, G.; He, X.; Helbig, N.; Holzwarth, N.; Jia, Y.; Jollet, F.; Lafargue-Dit-Hauret, W.; Lejaeghere, K.; Marques, M. A. L.; Martin, A.; Martins, C.; Miranda, H. P. C.; Naccarato, F.; Persson, K.; Petretto, G.; Planes,

V.; Pouillon, Y.; Prokhorenko, S.; Ricci, F.; Rignanese, G.-M.; Romero, A. H.; Schmitt, M. M.; Torrent, M.; van Setten, M. J.; Van Troeye, B.; Verstraete, M. J.; Zerah, G.; Zwanziger, J. W. The Abinit Project: Impact, Environment and Recent Developments. *Comput. Phys. Commun.* **2020**, *248*, 107042.

(83) Hamann, D. R. Optimized Norm-Conserving Vanderbilt Pseudopotentials. *Phys. Rev. B: Condens. Matter Mater. Phys.* **2013**, *88*, 085117.

(84) Frisch, M. J.; Trucks, G. W.; Schlegel, H. B.; Scuseria, G. E.; Robb, M. A.; Cheeseman, J. R.; Scalmani, G.; Barone, V.; Mennucci, B.; Petersson, G. A.; Nakatsuji, H.; Caricato, M.; Li, X.; Hratchian, H. P.; Izmaylov, A. F.; Bloino, J.; Zheng, G.; Sonnenberg, J. L.; Hada, M.; Ehara, M.; Toyota, K.; Fukuda, R.; Hasegawa, J.; Ishida, M.; Nakajima, T.; Honda, Y.; Kitao, O.; Nakai, H.; Vreven, T.; Montgomery, J. A., Jr.; Peralta, J. E.; Ogliaro, F.; Bearpark, M.; Heyd, J. J.; Brothers, E.; Kudin, K. N.; Staroverov, V. N.; Kobayashi, R.; Normand, J.; Raghavachari, K.; Rendell, A.; Burant, J. C.; Iyengar, S. S.; Tomasi, J.; Cossi, M.; Rega, N.; Millam, J. M.; Klene, M.; Knox, J. E.; Cross, J. B.; Bakken, V.; Adamo, C.; Jaramillo, J.; Gomperts, R.; Stratmann, R. E.; Yazyev, O.; Austin, A. J.; Cammi, R.; Pomelli, C.; Ochterski, J. W.; Martin, R. L.; Morokuma, K.; Zakrzewski, V. G.; Voth, G. A.; Salvador, P.; Dannenberg, J. J.; Dapprich, S.; Daniels, A. D.; Farkas, Ö.; Foresman, J. B.; Ortiz, J. V.; Cioslowski, J.; Fox, D. J. *Gaussian 09*, Revision E.01; Gaussian Inc.: Wallingford CT, 2013.

(85) Kresse, G.; Furthmüller, J. Efficiency of Ab-Initio Total Energy Calculations for Metals and Semiconductors Using a Plane-Wave Basis Set. *Comput. Mater. Sci.* **1996**, *6*, 15–50.

(86) Kresse, G.; Furthmüller, J. Efficient Iterative Schemes for Ab Initio Total-Energy Calculations Using a Plane-Wave Basis Set. *Phys. Rev. B: Condens. Matter Mater. Phys.* **1996**, *54*, 11169.

(87) Kresse, G.; Joubert, D. From Ultrasoft Pseudopotentials to the Projector Augmented-Wave Method. *Phys. Rev. B: Condens. Matter Mater. Phys.* **1999**, *59*, 1758–1775.

(88) Koopmans, T. Über die Zuordnung von Wellenfunktionen und Eigenwerten zu den Einzelnen Elektronen Eines Atoms. *Physica* **1934**, *1*, 104–113.

(89) Gonzalez, N.; Lorente, N.; Arnau, A. Methylthiolate Adsorption on Au(111): Energetics, Vibrational Modes and STM imaging. *Surf. Sci.* **2006**, *600*, 4039–4043.

(90) Tkatchenko, A.; Scheffler, M. Accurate Molecular Van Der Waals Interactions from Ground-State Electron Density and Free-Atom Reference Data. *Phys. Rev. Lett.* **2009**, *102*, 073005.

(91) Tonigold, K.; Gross, A. Adsorption of Small Aromatic Molecules on the (111) Surfaces of Noble Metals: A Density Functional Theory Study with Semiempirical Corrections for Dispersion Effects. *J. Chem. Phys.* **2010**, *132*, 224701.

(92) Mercurio, G.; McNellis, E. R.; Martin, I.; Hagen, S.; Leyssner, F.; Soubatch, S.; Meyer, J.; Wolf, M.; Tegeder, P.; Tautz, F. S.; Reuter, K. Structure and Energetics of Azobenzene on Ag(111): Benchmarking Semiempirical Dispersion Correction Approaches. *Phys. Rev. Lett.* **2010**, *104*, 036102.

(93) Stradi, D.; Barja, S.; Diaz, C.; Garnica, M.; Borca, B.; Hinarejos, J. J.; Sanchez-Portal, D.; Alcamí, M.; Arnau, A.; Vazquez de Parga, A. L.; Miranda, R.; Martin, F. Role of Dispersion Forces in the Structure of Graphene Monolayers on Ru Surfaces. *Phys. Rev. Lett.* **2011**, *106*, 186102.

(94) Faraggi, M. N.; Jiang, N.; Gonzalez-Lakunza, N.; Langner, A.; Stephanow, S.; Kern, K.; Arnau, A. Bonding and Charge Transfer in Metal-Organic Coordination Networks on Au(111) with Strong Acceptor Molecules. *J. Phys. Chem. C* **2012**, *116*, 24558–24565.

(95) Mercurio, G.; Maurer, R. J.; Liu, W.; Hagen, S.; Leyssner, F.; Tegeder, P.; Meyer, J.; Tkatchenko, A.; Soubatch, S.; Reuter, K.; Tautz, F. S. Quantification of Finite-Temperature Effects on Adsorption Geometries of  $\pi$ -Conjugated Molecules: Azobenzene/Ag(111). *Phys. Rev. B: Condens. Matter Mater. Phys.* **2013**, *88*, 035421.

(96) Díaz-Tendero, S.; Alcamí, M.; Martín, F. Density Functional Theory Study of the Structure and Vibrational Modes of Acrylonitrile Adsorbed on Cu(100). *Phys. Chem. Chem. Phys.* **2013**, *15*, 1288–1295.

- (97) Robledo, M.; Díaz-Tendero, S. Exploring the Adsorption and the Potential Energy Surface of Acrylonitrile on Cu(100) and Cu(100) Coated with NaCl Layers. *J. Phys. Chem. C* **2015**, *119*, 15125–15136.
- (98) Robledo, M.; Pacchioni, G.; Martín, F.; Alcamí, M.; Díaz-Tendero, S. Adsorption of Benzene on Cu(100) and on Cu(100) Covered with an Ultrathin NaCl Film: Molecule-Substrate Interaction and Decoupling. *J. Phys. Chem. C* **2015**, *119*, 4062–4071.
- (99) Rodríguez-Fernández, J.; Robledo, M.; Lauwaet, K.; Martín-Jiménez, A.; Cirera, B.; Calleja, F.; Díaz-Tendero, S.; Alcamí, M.; Floreano, L.; Domínguez-Rivera, M.; Vázquez de Parga, A. L.; Ecíja, D.; Gallego, J. M.; Miranda, R.; Martín, F.; Otero, R. Tuning Intermolecular Charge Transfer in Donor-Acceptor Two-Dimensional Crystals on Metal Surfaces. *J. Phys. Chem. C* **2017**, *121*, 23505–23510.
- (100) Schiavo, E.; Muñoz-García, A. B.; Barone, V.; Vittadini, A.; Casarin, M.; Forrer, D.; Pavone, M. Tuning Dispersion Correction in DFT-D2 for Metal-Molecule Interactions: A Tailored Reparameterization Strategy for the Adsorption of Aromatic Systems on Ag(111). *Chem. Phys. Lett.* **2018**, *693*, 28–33.
- (101) Schiavo, E.; Muñoz-García, A. B.; Maddalena, P.; Crescenzi, O.; Pavone, M. Doped Graphene and Ag(111) Hybrid Material as Fuel Cell Electrode: New Insights on Interfacial Features and Oxygen Adsorption from Dispersion-Corrected Density Functional Theory. *Comput. Mater. Sci.* **2019**, *169*, 109141.
- (102) Barzaga, R.; Hernández, M. P.; Aguilar-Galindo, F.; Díaz-Tendero, S. Revealing the Interplay Between Covalent and Non-Covalent Interactions Driving the Adsorption of Monosubstituted Thiourea Derivatives on the Au(111) Surface. *J. Phys. Chem. C* **2020**, *124*, 9924–9939.
- (103) Chulkov, E. V.; Silkin, V. M.; Echenique, P. M. Image Potential States on Metal Surfaces: Binding Energies and Wavefunctions. *Surf. Sci.* **1999**, *437*, 330–352.
- (104) Echenique, P. M.; Berndt, R.; Chulkov, E. V.; Fauster, T.; Goldmann, A.; Höfer, U. Decay of Electronic Excitations at Metal Surfaces. *Surf. Sci. Rep.* **2004**, *52*, 219–317.
- (105) Neuhauser, D.; Baer, M. The Application of Wave Packets to Reactive Atom–Diatom Systems: A New Approach. *J. Chem. Phys.* **1989**, *91*, 4651–4657.
- (106) Kroes, G. J.; Neuhauser, D. Avoiding Long Propagation Times in Wave Packet Calculations on Scattering with Resonances: A Hybrid Approach Involving the Lanczos Method. *J. Chem. Phys.* **1996**, *105*, 9104–9114.
- (107) Dion, M.; Rydberg, H.; Schröder, E.; Langreth, D. C.; Lundqvist, B. I. Van der Waals density functional for general geometries. *Phys. Rev. Lett.* **2004**, *92*, 246401.
- (108) Román-Pérez, G.; Soler, J. M. Efficient implementation of a van der Waals density functional: application to double-wall carbon nanotubes. *Phys. Rev. Lett.* **2009**, *103*, 096102.
- (109) Klimeš, J.; Bowler, D. R.; Michaelides, A. Chemical accuracy for the van der Waals density functional. *J. Phys.: Condens. Matter* **2010**, *22*, 022201.
- (110) Klimeš, J.; Bowler, D. R.; Michaelides, A. Van der Waals density functionals applied to solids. *Phys. Rev. B: Condens. Matter Mater. Phys.* **2011**, *83*, 195131.
- (111) Gauyacq, J. P.; Borisov, A. G.; Bauer, M. Excited states in the alkali/noble metal surface systems: A model system for the study of charge transfer dynamics at surfaces. *Prog. Surf. Sci.* **2007**, *82*, 244–292.
- (112) Borisov, A. G.; Kazansky, A. K.; Gauyacq, J. P. Resonant Charge Transfer in Ion–Metal Surface Collisions: Effect of a Projected Band Gap in the H<sup>+</sup>–Cu(111) System. *Phys. Rev. B: Condens. Matter Mater. Phys.* **1999**, *59*, 10935–10949.
- (113) Gauyacq, J. P.; Borisov, A. G. Excited electron transfer between a core-excited Ar\*(2p<sub>3/2</sub><sup>−1</sup>4s) atom and the metal substrate in the Ar/Cu(111) system. *Phys. Rev. B: Condens. Matter Mater. Phys.* **2004**, *69*, 235408.
- (114) Díaz-Tendero, S.; Borisov, A. G.; Gauyacq, J.-P. Theoretical Study of the Electronic Excited States in Ultrathin Ionic Layers Supported on Metal Surfaces: NaCl/Cu(111). *Phys. Rev. B: Condens. Matter Mater. Phys.* **2011**, *83*, 115453.
- (115) Bardeen, J. Tunnelling from a Many-Particle Point of View. *Phys. Rev. Lett.* **1961**, *6*, 57–59.
- (116) Payne, M. C. Transfer Hamiltonian Description of Resonant Tunnelling. *J. Phys. C: Solid State Phys.* **1986**, *19*, 1145–1155.
- (117) Tersoff, J.; Hamann, D. R. Theory of the Scanning Tunneling Microscope. *Phys. Rev. B: Condens. Matter Mater. Phys.* **1985**, *31*, 805–813.
- (118) Cohen-Tannoudji, C.; Diu, B.; Laloe, F.; Ostrowsky, N.; Ostrowsky, D. *Quantum Mechanics*; Wiley-VCH Verlag GmbH, 2019.
- (119) Boutu, W.; Haessler, S.; Merdji, H.; Breger, P.; Waters, G.; Stankiewicz, M.; Frasinski, L. J.; Taieb, R.; Caillat, J.; Maquet, A.; Monchicourt, P.; Carre, B.; Salieres, P. Coherent Control of Attosecond Emission from Aligned Molecules. *Nat. Phys.* **2008**, *4*, 545–549.
- (120) Huppert, M.; Jordan, I.; Baykusheva, D.; von Conta, A.; Wörner, H. J. Attosecond Delays in Molecular Photoionization. *Phys. Rev. Lett.* **2016**, *117*, 093001.